Active fluctuations of cells reduce friction to enable fast and coherent collective migration

Marcel Jipp, Bente D. Wagner, Lisa Egbringhoff, Andreas Teichmann, Angela Rübeling, Paul Nieschwitz, Alf Honigmann, Alexey Chizhik, Tabea A. Oswald, and Andreas Janshoff**

M. Jipp, B. D. Wagner, A. Teichmann, L. Egbringhoff, P. Nieschwitz, Prof. Dr. A. Janshoff
University of Göttingen, Institute of Physical Chemistry,
Tammannstr. 6, 37077 Göttingen, Germany
E-mail: ajansho@gwdg.de

A. Rübeling, Dr. T. A. Oswald
University of Göttingen, Institute of Organic and Biomolecular Chemistry,
Tammannstr. 2, 37077 Göttingen, Germany
E-mail: toswald@gwdg.de

Prof. Dr. A. Honigmann
Biotechnology Center, Technische Universität Dresden
Pfotenhauerstraße 108, 01307 Dresden, Germany

Dr. A. Chizhik
University of Göttingen, Third Institute of Physics
Friedrich-Hund-Platz 1, 37077 Göttingen, Germany

Keywords: tight junctions, traction force microscopy, collective cell migration, jamming, cell mechanics, atomic force microscopy

Abstract

Collective cell migration is an emergent phenomenon, with long-range cell-cell communication influenced by various factors, including transmission of forces, viscoelasticity of individual cells, substrate interactions, and mechanotransduction. We investigate how alterations in cell-substrate dynamics, cell-substrate adhesion, and traction forces impact in-plane fluidity and temporal-spatial correlation of confluent monolayers comprising wild-type MDCK II cells or ZO1/2-depleted MDCK II cells (dKD).
The combined data indicates that confluent dKD monolayers exhibit decreased in-plane fluidity compared to WT cells along with increased substrate adhesion, reduced traction forces, a more compact shape, diminished cell-cell interactions, and reduced cell-substrate height fluctuations. Depletion of basal actin and myosin further supports the notion that short-range cell-substrate interactions, particularly fluctuations driven by the basal actomyosin, significantly influence the migration speed of the monolayer on a larger length scale. Importantly, this in-plane fluidity proves to be highly compliant, requiring only a small portion of dynamic cells to maintain migration speed.

Introduction

Biological tissues emerge from long-range collective morphological transitions during development and regeneration. Diverse manifestations of collective cell migration exist, contingent upon the specific biological tissue and process.[1–4] In epithelial morphogenesis, wound healing, and regeneration processes, cells typically migrate in cohesive sheets attached to the extracellular matrix (ECM).[5,6] Perturbations of cellular motion lead to severe developmental defects, compromised wound healing, or even tumor formation.[1,7,8] Collective migration is a function of cell shape, cell-cell connectivity, cell-substrate adhesion, and active traction forces.[9,10]

Although the significance of adherens junctions (AJs) in creating contractile belts that connect cells into a seamless sheet and focal contacts formed between the cell's basal side and the extracellular matrix has been extensively demonstrated,[11–14] the importance of tight junctions (TJs) in the context of collective cell migration has only recently come under scrutiny. Tight junctions constitute multiprotein junctional complexes that create a seal between epithelial cells. Among the various proteins, peripheral membrane protein ZO-1 is crucial for actomyosin organization and contractility.[15] ZO-1 knockout (KO) cell lines exhibit an elevation in overall traction forces at the AJ due to the negative regulation of mechanical forces in the cells, leading to stronger cell-cell and cell-substrate forces.[16,17] Depletion of both ZO-1 and ZO-2 results in an even more noticeable phenotype. MDCK II cells reveal a dramatically thickened peri-junctional actin ring leading to an increased apicolateral tension directly at the cell junctions.[18–21] In contrast, apical surface tension in cell centers is decreased as excess surface area accumulates.[22,23]

Studies on the impact of functional tight junctions on cellular motility in migration have yielded conflicting evidence. KO studies targeting single ZO proteins have shown accelerated migration (ZO1[17]; ZO2[24]) and impaired migration (ZO1[25]; ZO3[17]) in different epithelial cells. However, cellular migration is severely compromised when cells lack the transmembrane TJ protein occludin[18] or a combination of ZO1 and ZO2[22] since force balance is disturbed. Further

studies showed that the balance between cellular contractility and differential adhesion between cells leads to a time-dependent demixing in WT/dKD confluent co-cultures.[26]

Here, we show that ZO-1/ZO-2 depleted cells display less coordinated movement of confluent cell monolayers than WT cells, even in a pre-jammed state. We attribute the loss of collective cell rearrangement to reduced actively driven cell-substrate-fluctuations (micromotion) along with lower traction forces to overcome cell-adhesion forces that are responsible for friction between substrate and cell monolayer. Our findings emphasize the requirement of sufficient cell-substrate dynamics to enable large-scale, coherently fluid movement of cells in mesoscale clusters.

Results

The impact of compromised tight junctions and altered cell-substrate interactions on the in-plane fluidity of MDCK II cells was assessed by a combination of phase contrast microscopy and particle image velocimetry (PIV).[27] Cells were cultivated on polyacrylamide gels (PAA), with a Young's modulus of 1.61 ± 0.01 kPa measured by atomic force microscopy (AFM). The gel substrate not only mimics native environments for cells but also enables us to quantify traction forces exerted by individual cells on the deformable substrate. The phase contrast videos reveal that confluent WT cells display higher in-plane fluidity than dKD monolayers (SI Videos and Figure 1A). The magnitude of velocity vectors from PIV was averaged to obtain the mean velocity of the entire cell layer over time, referred to as in-plane fluidity.

We examined intervals spanning all time frames (7.5 min/frame) commencing from the point at which confluency is reached (five hours after seeding). Overall, WT monolayers show a significantly higher in-plane fluidity of 21 ± 5 µm/h compared to dKD cells (15 ± 2 µm/h) at the point of confluence (Figure 1B). Throughout the observation period, the in-plane fluidity of both cell lines drops to a "baseline fluidity" (WT: 4.5 ± 1.0 µm/h, dKD: 4.7 ± 0.7 µm/h after 35 h) after about 25 h. This phenomenon can be explained by contact inhibition,[28] resulting in a gradual rise in cell density accompanied by an increase in eccentricity (SI-Figure 1), ultimately culminating in jamming.[29]

Hence, we also assessed the cell densities of the cell monolayers at different time points using the cell segmentation software Cellpose.[30] At elevated cell density, we expect the mobility of cells to diminish due to jamming as cells adopt a more compact shape, i.e., minimal perimeter at a given area.[31,32] We found that both cell lines initially have almost identical cell densities (WT: $1.8 \times 10^5 \pm 2.6 \times 10^4$ cells/cm^2, dKD: $1.9 \times 10^5 \pm 2.4 \times 10^4$ cells/cm^2) after reaching confluence (Figure 1C). Cell density increases with time for both cell lines until “baseline fluidity” is reached (after 20 h: $3.6 \times 10^5 \pm 5.4 \times 10^4$ cells/cm^2 (WT), $3.8 \times 10^5 \pm 7.6 \times 10^4$ cells/cm^2 (dKD)). After 40 h, however, the cell density of dKD cells is about twofold higher than at the 20-hour interval ($8.9 \times 10^5 \pm 2.1 \times 10^5$ cells/cm^2). In contrast, the cell density of WT cells experienced only a modest increase after attaining "baseline fluidity" (40 hours: $5.1 \times 10^5 \pm 1.3 \times 10^5$ cells/cm^2), suggesting that the differences in monolayer fluidity are not a result of differences in cell density. Despite the twofold increase in cell density for dKD cells, there is no substantial decrease in monolayer fluidity after 40 hours, reaffirming the presence of density- and shape-independent "baseline fluidity."

Fluidity extends beyond the collective 2D migration of cells within a plane; it also comprises the orthogonal motility of cells along the normal plane, essential for the dynamic opening and closing of adhesion bonds formed with the ECM. Therefore, we used electrical cell-substrate impendence sensing to monitor cell-substrate-fluctuations as a function of time. Impendence spectra of WT and dKD cell monolayer are shown in SI-Figure 3C and a frequency of 4 kHz is chosen to record cell-substrate-fluctuations of the cells cultured on the gold electrode (SI-Figure 3D. The complex impendence is expressed as a resistor in series to a capacitor. Cell-substrate-fluctuations are measured as resistance fluctuations. At frequencies ≤ 4 kHz the current flow is mainly between the cells and substrate as well as between cells.[33–35] Confirmed by optical inspection, the confluence of the cell layer was determined based on the point at which the overall resistance reached a plateau (black line in Figure 1D). Only the first 25 h after confluency were considered for subsequent analysis (Figure 1E, top). These trimmed data sets contain both cell-substrate-fluctuations and an overall long-term trend due to maturation of the monolayer, which was removed by empirical mode decomposition (EMD, SI-Figure 2A).[36–38] Subtracting the lowest-frequency modes from the original signal results in a detrended signal (Figure 1E, lower plot), which can be used to obtain the variance and temporal persistence (Figure 1F, SI-Figure 2D).[39] While the variance corresponds to the fluctuation amplitude, the scaling exponent of the detrended fluctuation analysis (DFA), α reflects the time series' self-correlations. At frequencies below 4 kHz, the WT cell layers show a higher variance ($3.2 \times 10^5 \pm 1.0 \times 10^5\ \Omega^2$) of the cell-substrate-fluctuations compared to dKD cells ($8.0 \times 10^4 \pm 4.0 \times 10^4\ \Omega^2$) and a higher α-value (WT: 1.47 ± 0.30, dKD: 1.16 ± 0.13). This indicates that more substantial, actively driven cell-substrate-fluctuations of the cleft between WT cells and substrate occur compared to dKD cells. At the same time, the larger α-values reflect the emergence of temporal persistence correlations (persistent motion) only for WT cells. We also compared the cell densities in the ECIS chambers with the in-plane fluidity measurements. Both WT ($2.6 \times 10^5 \pm 2.0 \times 10^4$ cells/cm^2) and dKD ($2.5 \times 10^5 \pm 1.2 \times 10^4$ cells/cm^2) have similar cell densities at the beginning of the ECIS measurement as well as in the in-plane fluidity measurements after 10 h (WT: $2.3 \times 10^5 \pm 2.5 \times 10^4$ cells/cm^2, dKD: $2.4 \times 10^5 \pm 3.0 \times 10^4$ cells/cm^2). Additionally, we performed impedance measurements with a doubled cell density to examine the cell-substrate-fluctuations of denser monolayers (SI-Figure 2B). Both cell lines display smaller variances compared to the lower-density monolayers, going hand in hand with the findings of decreasing in-plane fluidity with increasing cell densities. We found that in-plane fluidity and cell-substrate-fluctuations are highly correlated for WT cells. Changing the extracellular matrix composition results in altered cell-substrate-fluctuations and in-plane fluidity concomitantly. Conversely, dKD cells show almost no cell-substrate-fluctuations resulting in "baseline fluidity". The data (SI-Figure 3A) also confirms that cell-substrate-fluctuations dominate over resistance fluctuations originating from cell-cell-contacts.

In summary, dKD cells exhibit substantially lower in-plane fluidity and cell-substrate-fluctuations than WT cells. This decreased 3D mobility is already visible in the 25 hours after confluency but before jamming prevails. After this time point, the so-called "baseline fluidity" is reached, mainly reflecting a glassy state. The "baseline fluidity" does not require substantial cell-substrate-fluctuations. This is also evident in the vertical motion, where the denser WT and dKD monolayers exhibit diminished cell-substrate-fluctuations. While the in-plane movement can be explained by the contractile behavior of the dKD cells adopting a very compact shape, the altered cell-substrate-fluctuations remain unknown. It requires direct measurements of the basal activity, such as traction forces.

The average traction forces decrease with decreasing in-plane fluidity

The hypothesis is that the origin of cell-substrate-fluctuations is the actomyosin contractility of the cell. This is expected to be mirrored by cellular traction forces (Figure 2A) and the immunostaining of myosin (vide infra). We found that WT monolayers generated higher average traction forces (58 Pa ± 20 Pa) compared to dKD monolayers (40 Pa ± 7 Pa) 10 hours (cell density: 1.7 - 2.6 x 10^5 cells/cm^2) after reaching confluence (Figure 2B). The average traction forces also decrease with decreasing in-plane fluidity of the monolayers. After 20 h, WT monolayers exert average traction forces of 47 ± 13 Pa, while dKD show average traction forces of 38 ± 6 Pa (cell density: 2.8 – 4.5 x 10^5 cells/cm^2). The average traction forces drop further after 40 h (cell density: 5.5 – 8.0 x 10^5 cells/cm^2), with a more significant decrease in traction forces in the WT cell line (42 ± 10 Pa) than in the dKD cells (32 ± 13 Pa) also concurrent with the drop of in-plane fluidity.

We also performed traction force experiments in the presence of Mitomycin C (MitoC) to separate the impact of longer incubation time and density increase by blocking proliferation.[40,41] Monolayers were treated with MitoC after 20 hours and incubated for an additional 24 hours. The average traction forces of these MitoC-treated monolayers are slightly higher than untreated monolayers 20 hours after the point of confluence (Figure 6E). This proves that the cell layers do not reduce the average traction forces due to longer incubation time but rather when entering the jammed state as the cell density increases.

ZO-1/2 dKD cells show increased cell-substrate adhesion

We used single-cell force spectroscopy (via AFM) to examine whether cell-substrate adhesions can explain the reduced 3D mobility in dKD monolayers. A solitary cell was affixed to a cantilever without a tip and positioned in contact with a PAA gel for a specified duration to facilitate the formation of non-covalent bonds by the cell. Subsequently, the cell was disengaged from the surface, and the maximum force required for detachment was documented (Figure 2C). WT cells exhibited slightly lower cell-substrate adhesion forces after a contact time of 150 s compared to dKD cells (Figure 2D). As this method is extremely precise but cannot be used for longer incubation times due to the elevated forces, we also used a centrifuge assay to quantify the fraction of cells that withstand rupture during centrifugation.[42,43] With increasing cell numbers remaining on the substrate after experiencing centripetal forces, stronger cell-substrate adhesion forces per area are consequently assumed. We analyzed phase-contrast images before and after centrifugation with incubation times of 10 and 20 minutes prior to spinning to obtain the fraction of adherent cells. We observed higher fractions of adherent cells in dKD samples (19.5 ± 4.2 %) compared to WT cells (10.4 ± 2.2 %) after 10 minutes, suggesting that dKD cells provide larger adhesion forces per area. The fraction of cells remaining on the substrate increases after an incubation time of 20 minutes for both cell lines. AFM and centrifugation assays demonstrate that traction forces and cell-substrate adhesions do not go hand in hand but confirm larger stick-slip frictional forces for dKD cells generated by ligand-receptor bonds formed in the contact zone.[44] We assume that myosin activity generating piconewton pulling forces is responsible for the reduced number of bonds in WT cells.

Contractility switch on the basal side

Previous studies have shown that cells lacking ZO-1/2 are more contractile and express an increased apical actomyosin ring, while WT cells do not show any upregulation.[21,22] It therefore seems counterintuitive that the traction forces are reduced in these contractile cells. Consequently, we used confocal fluorescence microscopy to visualize both F-actin and myosin light chain kinase, essential proteins of the basal actomyosin skeleton, which is critically involved in generating cellular traction forces.[45,46]

The increased apical actomyosin ring can also be seen in dKD cells cultured on PAA substrates (small figures in the right corners in Figure 3A). However, we observed structural changes in the actomyosin skeleton on the basal side of the monolayers. dKD cells revealed, on average, 46% lower myosin intensity and 24% lower actin intensity than WT cells (Figure 3B). Higher fluorescence intensity indicates increased activity of myosin and actin on the basal side, correlating with the differences in traction force data. As a result, an increase in myosin and actin activity on the basal cell side is associated with higher average traction forces in the monolayer.

Less traction force and higher adhesion force should result in an altered cell-substrate distance. To quantify this, we performed membrane height studies with both cell lines using metal-induced energy transfer (MIET) microscopy, providing unprecedented nanometer z-resolution, allowing a spatial inspection of the cleft between the basal cell side and the gold substrate.[47–51] For membrane height quantification, we selected six rectangles in the center of a cell from each measurement (Figure 3C). The extracted points obtained from each of these rectangles were averaged. We found that the WT cells have an average height of (159 ± 12 nm), while the dKD cells were closer to the substrate, with an average height of (116 ± 14 nm) (Figure 3D).

Our findings show a contractility switch between the apical and basal sides of the cells. The lower actin and myosin intensities of dKD cells indicate a lower basal contractility, explaining the reduced traction forces of the dKD monolayers. Moreover, with lower cell-substrate-fluctuations of the basal side, the dKD monolayers are, on average, closer to the substrate.

Actomyosin activity governs the dynamics of individual cells and thereby steers collective migration

To further validate the hypothesis of diminished basal contractility in confluent dKD cells compared to WT cells, we conducted experiments using Blebbistatin (Blebb), a selective inhibitor of myosin-II, to stall the overall cortical contractility.[52] We found a decreased collective in-plane movement of confluent monolayers treated with 50 µM Blebb over time (Figure 4A + 4B). The in-plane fluidity of WT cells decreased from 17 ± 3.8 µm/h after 5 hours to merely 9.2 ± 3.1 µm/h after 20 hours. In contrast, dKD cells were slower throughout the entire observation time. Their velocity was 12 ± 3.4 µm/h after 5 hours and decreased to 4.8 ± 0.7 µm/h after 20 hours. The cell density remains almost constant during the observed period (Figure 4C).

Concomitantly, the cell-substrate-fluctuations also drop substantially in response to myosin II inhibition (Figure 4D). The WT monolayers display a slightly higher variance of the cell-substrate-fluctuations ($3.3 \times 10^4 \pm 1.6 \times 10^4\ \Omega^2$) compared to dKD cells ($9.1 \times 10^3 \pm 6.6 \times 10^3$

Ω^2) in the presence of Blebb, which are probably thermally excited membrane/cortex undulations. We, therefore, ascertain that diminishing the basal actomyosin cytoskeleton's contractility hinders the cells' capacity to engage in significant z-movements to generate traction forces and, consequently, hampers collective cell migration.

Interestingly, as the cells' contractile ability diminishes, both WT and dKD cells reveal a similar decrease in in-plane fluidity. This suggests that the initial variations in cell motility and dynamics arise from the contractile machinery of the basal actomyosin cytoskeleton. Suppressing myosin II activity in WT cells eliminates these differences, leading to a convergence in behavior between WT and dKD cells. The importance of basal contractility is further supported by measuring the distance between the basal membrane and the substrate using MIET microscopy (Figure 4E). Following Blebb treatment, the average height of the basal membrane in WT cells is 116 ± 23 nm. Consequently, this aligns with the basal membrane height of dKD cells without Blebb treatment (116 ± 14 nm). Essentially, the inhibition of myosin II in dKD cells does not affect the distance between the substrate and membrane, remaining very similar at 126 ± 21 nm. This indicates that the larger distance between the substrate and basal membrane in WT cells compared to dKD cells is actively driven by the basal actomyosin.

A similar trend is also found for the traction forces exerted by the cells on the substrate. Both WT (22 ± 10 Pa) and dKD (20 ± 8.0 Pa) cells show similar traction forces after treatment with Blebb (Figure 4F), substantially reduced compared to untreated control cells. We averaged the traction forces between 10 h and 20 h to include more data points. This observation emphasizes that reduction of the basal contractility of WT cells causes a comparable phenotype to untreated dKD cells in which basal contractility is reduced, leading to reduced cell-substrate-fluctuations.

Interestingly, cell-substrate adhesion forces are only slightly influenced by the reduction of contractility (Figure 4G), i.e., we noted a marginal increase in adhesion forces in WT (0.9 ± 0.7 nN) and dKD (1.6 ± 1.0 nN), respectively, showing again that adhesion forces are not correlated with traction forces.

We deduce that the effective friction between the substrate and the basal cell membrane is diminished in WT cells due to increased contractility of the basal actomyosin network compared to dKD cells. This results in elevated micromotion amplitude, temporal persistence, and increased overall traction forces. Eventually, reduced friction with the substrate leads to higher collective migration speed and coherence. WT cells resemble dKD phenotypes after treatment with Blebb, showing reduced 3D fluidity and traction forces upon reduction of basal contractility.

Rho activation rescues the basal actomyosin cytoskeleton of dKD

Can the reduced basal contractility of dKD cells be rescued by stimulating the Rho pathway? To answer this question, we used the Rho activator CN03 (1 µg/mL), which increases stress fiber number and order.[10] In-plane fluidity does not change over time compared to untreated monolayers (Figure 5A). In contrast, the cell-substrate-fluctuations are dramatically reduced (Figure 5B). The variance of CN03-treated WT monolayers ($5.9 \times 10^4 \pm 2.2 \times 10^4\ \Omega^2$) dropped to the level of untreated dKD cells ($8.0 \times 10^4 \pm 4.0 \times 10^4\ \Omega^2$, Figure 1F). CN03-treated dKD

monolayers ($1.3 \times 10^4 \pm 5.1 \times 10^3\ \Omega^2$) also show less cell-substrate-fluctuations than untreated ones.

Besides, the basal membranes of both cell lines are, on average, substantially closer to the substrate (Figure 6C). WT basal membranes with CN03 treatment (59 ± 11 nm) are more than twice as close to the substrate than untreated WT cells (159 ± 12 nm). Also, the dKD cells are significantly closer to the substrate with 70 ± 14 nm.
This is further rationalized by fluorescence images of actin on the basal side before and after treatment with CN03 (Figure 5D). In response to Rho activation, the basal intensity of actin in dKD monolayers (1124 ± 196 a. u.) reaches the same level as the untreated WT monolayers (1129 ± 132 a. u.), while the CN03-treated WT monolayers (1284 ± 203 a. u.) show only a small increase in actin intensity (Figure 6E). This means we can reestablish the loss of basal contractility in dKD monolayers by administering CN03.

In the next step, we performed traction force experiments with CN03-treated monolayers. We averaged traction force data sets collected between 10 h and 20 h after seeding (Figure 5F). We found that, on average, CN03-treated dKD monolayers generate higher traction forces (97 ± 14 Pa) than untreated cells. The traction forces of WT monolayers are also insignificantly affected (CN03 treatment: 79 ± 20 Pa). Both data sets show a correlation between actin intensity and traction forces with larger traction forces on average coupling with higher actin intensity.

These findings indicate that Rho activation leads to more stress fibers, increasing basal contractility and traction forces that essentially iron out micromotion and pull the cells closer to the substrate. However, to our surprise, the cells maintain their collective in-plane fluidity, with neither the WT cells slowing down nor the dKD cells gaining speed. This implies that the cells compensate for decreased out-of-plane dynamics by stronger traction forces that overcome increased friction.

In-plane movements are collective on a larger scale, while vertical movements are more individual on short-length scales

We also examined a co-culture (1:1 mixtures of WT and dKD) using optical microscopy and ECIS to quantify how the interactions between the contractile dKD cells and the intrinsically less contractile WT cells alter cell-substrate-fluctuations and in-plane fluidity. At the point of confluence, the co-culture exhibited a slightly reduced in-plane fluidity (18 ± 1.0 µm/h) compared to WT monolayers (Figure 1B) while converging to the behavior of WT over the observation period. This indicates that the overall in-plane movement of the monolayer does not depend on individual cells but is caused collectively by the cell layer capable of largely compensating for slower cells.

Interestingly, the co-culture behaves differently in cell-substrate-fluctuations assessed by ECIS. The variances of the detrended signals ($1.8 \times 10^5 \pm 9.0 \times 10^4\ \Omega^2$) are in the range between the WT and dKD cultures (Figure 1F) as expected from the mixing ratio of cells. Hence, the data indicates that cell-substrate-fluctuations of the cell layer are more individualized, manifesting on shorter length scales as no compensation from WT cells occurs. To study this further, we adjusted WT/dKD ratios in the co-culture (SI-Figure 2C) and observed a reduction in cell-substrate-fluctuations with increasing dKD ratio. This indicates that vertical movement does

not reflect the collective behavior of the monolayer but occurs on the level of single cells. However, elevated cell-substrate-fluctuations are essential to reduce friction with the substrate in a fraction of cells to maintain in-plane fluidity.

Traction forces of confluent dKD and WT MDCK II cells in co-culture

Furthermore, we also determined the traction forces of co-cultures with different WT/dKD ratios at different times (Figure 6A). For the differentiation and segmentation of WT and dKD cells in the monolayer, we used WT cells with a myosin-GFP tag (WT-GFP) as detailed elsewhere.[22] To ensure that WT-GFP cells have comparable average traction forces as WT (65 ± 18 Pa), we determined the traction forces of WT-GFP monolayer between 10 and 20 hours after the point of confluence (59 ± 12 Pa, Figure 6D). A representative traction force map of the co-culture for both times is shown in Figure 6A. Within the co-culture, WT-GFP cells generated higher traction forces on average than dKD cells (Figure 6B). As anticipated, the average traction forces of the confluent co-culture rise in correlation with the area covered by WT-GFP cells (Figure 6C) 20 hours after reaching confluence, whereas this dependence is less prominent after 40 hours. This reduced effect can be attributed to the elevated cell density, as observed in monoculture experiments (Figure 2B).

Cluster sizes correlate with in-plane movements

A cluster size analysis of the cell monolayers was carried out to quantify the spatial coherency of monolayer fluidity (Figure 7A). Early (between 5 and 10 h after seeding) and late (jammed) (between 30 and 35 h after seeding) phases of the observation period were examined. Cells moving in the same direction are gathered into a cluster, with larger clusters indicating a more pronounced coherent movement. WT cells (1296 ± 245 μm^2) and co-cultures (1103 ± 223 μm^2) form bigger clusters than dKD cells (921 ± 188 μm^2) in the early phase (Figure 7B, upper plot). Average cluster sizes of mono- and co-culture decrease over time, with WT cells converging to 667 ± 482 μm^2, while dKD (650 ± 369 μm^2) and co-culture (497 ± 226 μm^2) form smaller clusters (Figure 7B, lower plot). The decay of lateral velocity correlation (Figure 7C) in early phases in WT was shorter than that in dKD and co-culture, as indicated by a longer correlation length for WT (62.6 ± 17.5 μm) compared to dKD (45.6 ± 4.8 μm) and co-culture (55.2 ± 6.3 μm). Additionally, we analyzed mean square displacements (MSD) for monolayers during early phases (Figure 7D) to assess their rearrangement capabilities. Generally, WT cells exhibit higher MSDs than dKD cells, with the co-culture at an intermediate level. The MSD ($MSD \propto \tau^{\alpha}$) allows us to deduce cell rearrangement activity from the scaling exponent (α) for different cell lines and conditions. An α value of 2 suggests linear movement, while α = 1 indicates Brownian motion, and smaller values imply enhanced friction by neighboring cells leading to subdiffusive motion. The MSD exponent is higher for WT (1.23 ± 0.04), indicative of superdiffusive motion compared to dKD (1.02 ± 0.04) and co-culture (1.12 ± 0.03). As cell density increases, the exponents decrease, suggesting decreased mobility as cells approach the jamming limit, aligning with previous research.[10,22]

Discussion

The concept of collective migration surpasses the mere coordinated movement of individual cells.[2] Thus, the crux of collective cell migration lies in the cells' capacity to reposition themselves relative to their neighbors with minimal substrate friction. The shape of cells expedites cellular reorganizations, as those with elongated forms and larger perimeters can more readily glide past neighboring cells within the cell layer.[1,10,32,53–56] While it is believed that cortical tension and adhesion at the periphery of each cell predominantly regulate cell perimeter, experimental investigations into this hypothesis have yielded contradictory outcomes.[10] The conflicting results have recently been resolved by examining forces, cell perimeters, and motion of an epithelial monolayer as a function of cell density.[10] The authors observed a simultaneous decrease in all three factors with elevated cell density or the inhibition of cell contraction. Interestingly, the augmentation of tractions was identified as a factor capable of counteracting the influence of density on cell shape and rearrangements. Consequently, their study shifts the emphasis away from cell-cell contacts, highlighting cell-substrate traction as a primary physical determinant governing shape and motion in collective cell migration.

Here, we extend this picture by adding out-of-plane dynamics using two cell lines that differ substantially in collective migration. Our findings imply that the orchestration of rearrangements and coherency is governed by stress fibers, which exert tractions at the cell-substrate interface, and active, long-term fluctuations of the cell shape that lift motile cells over the surface as if at elevated temperature. We use two different cell lines, WT (MDCK II cells) and dKD (MDCK II cells), in which ZO1/2 are depreciated. Loss of functional TJs leads to an imbalance in the actomyosin skeleton on soft polyacrylamide gels. A thick, highly contractile actomyosin ring is formed on the apical side in dKD cells, sacrificing basal contractility, which is especially pronounced in later stages when jamming occurs. It is assumed that TJs exert negative mechanical feedback on the actomyosin cytoskeleton of individual cells in a cell layer.[16] This feedback function helps to prevent excessive contraction and elongation of the cells and, therefore, maintains tissue integrity. In the TJ-KO cell lines, it has been observed that this feedback loop is missing, leading to uncontrolled contraction.[16,22] In contrast, little is known about the basal actomyosin skeleton in TJ-KO cells. We found pronounced actin and myosin gradients in dKD cells, suggesting reduced basal contractility as recently reported for glassy substrates.[26] The altered basal actomyosin skeleton in dKD cells explains the reduced average traction forces in dKD monolayers. The monolayers with higher density exerted lower traction forces on average regardless of the cell type, as also found by Saraswathibhatla et al.[10] We could rule out that proliferation is responsible for the observed alteration of traction forces but noticed that the average traction forces in the cell layer depend on the composition of the cell monolayer. The more dKD cells in the monolayer, the lower the average traction forces become, and cell-substrate-fluctuations are concomitantly reduced.

Furthermore, we show that confluent dKD monolayers exhibit reduced collective mobility paired with lower traction forces and a more compact shape. We further show that cell density and, therefore, average cell size is not the reason for the difference in in-plane fluidity of dKD cell layers and WT MDCK II cells. Nevertheless, we consistently confirm in-plane fluidity decreases in both cell lines as cell density rises.[31,32,54] Furthermore, monolayers with higher fluidity exerted higher average traction forces. Saraswathibhatla et al. identified analogous

correlations when examining cell layers with varying densities. Monolayers with higher cell density exhibited lower traction forces compared to low cell density.[10]

In the PIV data, we also observed a "baseline fluidity" of 4 µm/h, consistent with earlier findings.[31] After reaching "baseline fluidity", cell density in dKD cell layers still increases significantly, while it nearly does not change in WTs. This effect can be explained by the role of ZO proteins in controlling proliferation through cell cycle arrest.[57,58] Hence, when TJs are depleted, cells lose contact inhibition. Moreover, dKD cells show smaller cell clusters with coordinated movement, a lower scaling exponent of the MSD, and shorter correlation lengths indicative of reduced cell-cell force transmission. Importantly, WT cells display substantially larger cell-substrate-fluctuations paired with a larger cell-surface distance, allowing the cell to reduce friction to the substrate and respond swiftly to mechanosignalling. Fluctuations are found to be responsible for adjusting the average cell-substrate distance and, therefore, allowing the cells to remain in an out-of-equilibrium state.[59] Sabass and Schwarz showed how cell-substrate friction depends on the number of bonds, their dynamics, and intracellular relaxation.[60] In this state, only slight variations in control parameters, such as on/off rates of adhesion molecules, lead to significant changes in macroscopic quantities characterizing the system. This permits the cell to bridge length scales on short time scales by small variations in contractility. Elevated cell-substrate-fluctuations paired with increased average distance of the cell from the substrate are also found at the onset of the epithelial-to-mesenchymal transition (EMT), where cells enter a state of higher mobility, larger distance from the surface and more fusiform shape – all parameters allowing the cells to move more rapidly and independently.[49,61,62] An increase in cell density further reduces basal movement, which aligns with the observed lateral fluidity.[49] It is well known that migration and, therefore also, basal movement of the membrane is significantly influenced by myosin II.[63]

The short-range force transmission in cell clusters, resulting from cell-matrix adhesions, contrasts with the longer-range force transmission required for processes like collective cell migration. Active regulation of force propagation through spatial coordination of actomyosin contractility is proposed to achieve this longer-range force transmission, as seen in tissue morphogenesis.[64,65] The reduction in spatial and temporal persistence in confluent dKD cells before jamming results in compromised long-range force transmission, leading to slower and less coherent migration. This is further fostered by increased cell adhesion, which inhibits long-range transmission. Conversely, loosely attached cells can effectively relay forces, as we see with WT cells.[65]

Applying CN03 results in an elevated quantity of stress fibers and consequently augments traction forces, which could maintain in-plane fluidity even at reduced micromotion. Conversely, using blebbistatin decreases fluctuations down to thermal noise, reducing the fluidity of the cell layer.

The idea that shape fluctuations might foster 2D fluidity has recently been proposed by Manning and coworkers using tissue models.[66] According to Yanagida et al.'s research, the sorting of the primitive endoderm from the epiblast in the inner cell mass in early mammalian embryos is attributed to differential cell surface fluctuations rather than static physical parameters.[67]

Taken together, our results indicate that cells invest energy to maintain high in-plane fluidity by shape fluctuations beyond the thermal level. We also conclude from co-culture experiments that only a fraction of cells with elevated cell-substrate-fluctuations is needed to maintain collective in-plane fluidity.

Acknowledgements

Funding by the DFG through grant JA963/19-1 is gratefully acknowledged. The authors thank Burkhard Geil for the helpful discussions on image analysis, segmentation, tracking, and empirical mode decomposition. The authors would also like to acknowledge Jörg Enderlein for his assistance and expertise in MIET.

Conflict of Interest

The authors declare no conflict of interest

Star Methods

Key resources table

REAGENT or RESOURCE	SOURCE	IDENTIFIER
Antibodies		
phospho-myosin light chain 2 (Ser 19) rabbit IgG1	Cell Signaling Technology	Cat#3671
AlexaFluor 488-conjugated goat anti-rabbit IgG H&L 2 mg/ml	Abcam	Cat#ab150077
Bacterial and virus strains		

Biological samples		

Chemicals, peptides, and recombinant proteins		
MEM, GlutaMAX™ Supplement	Gibco™	Cat#41090093
Fetal Bovine Serum Premium (FBS)	biowest	Cat#S181B-500
Dulbecco's Phosphate Buffered Saline (PBS)	Gibco™	Cat#21600-051
Trypsin 2.5%	Gibco™	Cat#15090-046
Ethylenediaminetetraacetic acid (EDTA)	Invitrogen	Cat#AM9260G
Acrylamide (4x crist.)	Roth	Cat#A7906.1
N, N'-Methylen-bis-acrylamid, 99.5%	Sigma	Cat#M7279
3-Aminopropyltriethoxysilane (APTES)	abcr GmbH	Cat#AB110815
Glutaraldehyde 25 wt % (GDA)	Sigma	Cat#G5882
Ammonium persulfate (APS)	Carl Roth GmbH	Cat#9592.3
Tetramethylethylenediamine (TEMED)	Carl Roth	Cat#2367.3
Dichlorodimethylsilane	Merck	Car#8.03452
SULFO-Sanpah	Thermo Scientific™	Cat#22589
Collagen I (rat tail)	Ibidi	Cat#50201
Fibronectin	Sigma	Cat#F1141
Poly-L-lysine	Sigma	Cat#P5899
Laminin	Sigma	Cat#L2020
Hank's Balanced Salt Solution (HBSS)	Gibco	Cat#24020083
Acetic Acid 100% p.a.	Carl Roth	Cat#3738.4
Biotin-BSA	Thermo Scientific™	Cat#29130
Streptavidin	Sigma	Cat#S4762-5mg
Concanavalin A-biotin	Sigma	Cat#C2272-2mg
HEPES-solution	Sigma	Cat#H0887
Penicillin-Streptomycin	Sigma	Cat#P43333
CellMask™ Plasma Membrane Stain, Deep Red	Life Technologies	Cat#C10046
Paraformaldehyde (PFA)	Science Services	Cat#E15714
Para-amino-blebbistatin	Motorpharma	Lot: AmB-ChB-2
Rho Activator II, Deamidation of Rho Gln-63	Cytoskeleton, Inc.	Cat#CN03
Mitomycin C (MitoC)	Sigma	Cat#M4287-2MG
Normal Goat Serum	Life Technologies	Cat#PCN5000
Triton X-100	Sigma	Cat#T9284
AlexaFluor 546-phalloidin	Invitrogen	Cat#A22283
Critical commercial assays		

Deposited data		
Experimental models: Cell lines		
Madin-Darby Canine Kidney II Wild-type (WT)	ECACC	Cat#00062107
Madin-Darby Canine Kidney II (ZO-1/ZO-2 double-knockdown, dKD)	Gift from Prof. Honigmann[68]	N/A
Madin-Darby Canine Kidney II GFP-myosin-2-A (WT-GFP)	Generated as described[22]	N/A
Experimental models: Organisms/strains		
--		
Oligonucleotides		

Recombinant DNA		

Software and algorithms		
ImageJ Fiji	https://imagej.net/software/fiji/	N/A
ImageJ plug-in "Template Matching and Slice Alignment"	https://biii.eu/template-matching-and-slice-alignment-imagej-plugins	N/A
Keyence BZ-X800 Viewer	Keyence	N/A
Olympus Fluoview Ver. 4.2	Olympus	N/A
JPK Data Processing	JPK	N/A
Matlab R2020b	The MathWorks, Inc.	N/A
Matlab PIV	W. Thielicke[27]	https://www.mathworks.com/matlabcentral/fileexchange/27659-pivlab-particle-image-velocimetry-piv-tool-with-gui
Easy-to-use-TFM_package	Huang et al.[69]	https://github.com/CellMicroMechanics/Easy-to-use_TFM_package
Python 3		https://www.python.org/
Cellpose	Stringer et al.[30]	https://github.com/MouseLand/cellpose
MIET analysis software	Ghosh et al.[70]	https://projects.gwdg.de/projects/miet/
Python ECIS	Self-written	https://gitlab.gwdg.de/janshoff_lab
Centrifuge assay analysis	Self-written	https://gitlab.gwdg.de/janshoff_lab
Paul N.s Analyse Cluster analysis and MSC calculation	Self-written	https://gitlab.gwdg.de/janshoff_lab
Other		
Fluospheres, 0.2 µm, orange (540/560 nm)	Invitrogen	Cat#F8809
Petri dish (µ-dish 35 mm, high, glass bottom)	Ibidi	Cat#81158
Round cover glasses (13 mm diameter)	VWR	Cat#631-9508
ECIS Cultureware 8W1E PET	Ibidi	Cat#72001
MLCT-O10	Bruker AFM Probes	N/A

RESOURCE AVAILABILITY

Lead contact

Further information and requests for resources and reagents should be directed to and will be fulfilled by the lead contact, Andreas Janshoff (ajansho@gwdg.de).

Materials availability

This study did not generate new unique reagents.

Data and code availability

All data reported in this paper will be shared by the lead contact upon request.
Any additional information required to reanalyze the data reported in this paper is available from the lead contact upon request.

METHOD DETAILS

Cell culture

Madin-Darby Canine Kidney cells (strain II, MDCK II) were cultured in M10F$^-$ (Minimum Essential Medium (MEM) containing Earle's salts, 10% Fetal Bovine Serum Premium (FBS), 2 mM glutaMAX at 37 °C and 5% CO_2 in a humidified incubator. Cells were passaged every two to three days using phosphate buffered saline pH 7.4 (PBS$^-$) containing trypsin/EDTA (0.25%/0.02% w/v). The knockdown of ZO-1 and ZO-2 in MDCK II cells was done by Beutel et al. using CRISPR/Cas9.[68] MDCKII cells expressing GFP-myosin-2-A (WT-GFP) were generated as previously described by Skamrahl et al.[22]

Sample preparation and analysis

PAA gel preparation

A monomer stock solution (7.5% acrylamide (AA) and 0.075% N,N'-methylenebisacrylamide (Bis-AA)) was mixed in distilled water to prepare polyacrylamide (PAA) gels yielding a Young's modulus of 1.61 kPa. The bottom of a Petri dish (µ-dish, 35 mm, high, glass bottom) was incubated with 150 µL of 3-aminopropyltriethoxysilane (APTES) for 5 minutes and then rinsed three times with distilled water. Subsequently, the dried surface was treated with 200 µL 2.5% glutaraldehyde solution (GDA) in PBS^- for 30 minutes, followed by two rinses with distilled water. Coverslips (13 mm, borosilicate glass) were washed twice with isopropanol and then cleaned thoroughly using a plasma cleaner (Zepto, Diener Electronics, Ebhausen, Germany). They were then coated with dichlorodimethylsilane for 5 minutes. Finally, the coverslips were washed with 70% ethanol and distilled water and dried completely using nitrogen gas.

A solution of 4 µL fluorescent beads (Fluospheres, 0.2 µm, orange (540/560 nm) and 246 µL of the monomer stock solution was homogenized using a sonicator for 30 min. Then, 2.5 µL ammonium persulfate (APS, 1 mg/10 µL) and 0.5 µL tetramethylethylenediamine (TEMED) were added to the solution and mixed thoroughly. 6 µL of the solution was added to each prepared Petri dish, covered with a coverslip, and allowed to polymerize for 45 min in a humid atmosphere. The coverslip was carefully removed after the gel was fully polymerized.

200 µL SULFO-Sanpah solution (0.5 mg/mL) was added to the gels and exposed to UV light (365 nm) for 8 min. Subsequently, the gels were rinsed with distilled water. These steps were repeated twice. Afterward, the gels were coated with collagen (1 µL of collagen I (rat tail in PBS^-), 5 mg/mL in 199 µL PBS^- with 0.02 M acetic acid) for one hour at room temperature. The gels were stored for further use in distilled water at 4°C.

Migration assay

For the migration experiments, Petri dishes containing PAA gel without fluorescent beads were used onto which 5 x 10^5 cells (for co-culture, a 1:1 mixture of WT/dKD was used) were seeded in 300 µL $M10F^-$, to ensure the cells only attach to the gel. After 2 hours, the cells were rinsed with $M10F^-$ before 2 mL was added for incubation and imaging. Three to four hours after seeding, the cells were placed in the incubation system (Uno-T-H-CO2; Okolab S.R.L., Pozzuoli NA, Italy) mounted on an inverted optical microscope (BZ-X810; Keyence, Neu-Isenburg, Germany) equipped with a 20× phase-contrast objective (Plan Fluor ELWD 20x; Nikon Europe B.V., Amstelveen, The Netherlands). The incubation chamber was operated at 37 °C and 5 % CO_2 with sufficient humidity. Phase contrast images were acquired every 7.5 min over a period of 48 h. Focus tracking was applied, and three vertical images were selected in a range of 8 µm to account for vertical drift effects, of which the best-focused images were selected manually for analysis. The phase contrast videos obtained were analyzed using particle image velocimetry (PIV) with the MATLAB application PIVlab to compute the velocity vectors of each frame.[27] The velocity vectors were generated with an interrogation window of 64 x 64 pixels (49.28 x 49.28 μm^2), and overall in-plane fluidity was defined as the mean velocity vectors in one frame. Mean and standard deviation were determined from independent experiments: WT (m = 27, n = 9), dKD (m = 22, n = 6), co-culture (m = 12, n = 2), WT + Blebb (m = 15, n = 4), dKD + Blebb (m = 12, n = 4), WT + CN03 (m = 6, n = 1), dKD + CN03 (m = 6, n = 1).

Cell segmentation

The Cellpose cell segmentation algorithm was used to generate a mask for each cell.[30] To accurately capture all cells in the layer, parameters for flow and cell probability were set to 1 and -6, respectively. Each cell's diameter (short and long axis) and the cell density in one frame were then calculated from the cell masks obtained from each frame.

Eccentricity analysis

The eccentricity (defined as the ratio of the length of the short (minor) axis to the length of the long (major) axis) was calculated from the Cellpose data and averaged for each frame. Mean and standard deviation were determined from independent experiments: WT (m = 18, n = 5), dKD (m = 15, n = 4), WT + CN03 (m = 6, n = 1), dKD + CN03 (m = 6, n = 1).

Cluster Analysis and MSD

A self-written optical flow analysis implemented in Python was used for cluster analysis and MSD calculations. It is based on an algorithm introduced by Gunnar Farnebäck.[71] The algorithm is tuned using two Gaussian kernel parameters, one for blurring the images in the polynomial fitting step and one for the flow field's smoothness in the algorithm's weighted neighborhood estimation. An example image from the video stack is rotated by a defined angle to find the best-suited parameters. Then, the difference between the analytical displacement field and the calculated result from the optical flow algorithm is calculated for multiple sets of parameters. A set of parameters is found reasonable when the standard deviation between the two fields is of the order of 0.3 px. Typical parameters are $\sigma = 4$ for the blurring kernel and $\sigma_{\text{flow}} = 2$ for the flow field kernel. Additionally, the images are sharpened before optical flow calculation by adding the difference between the original and a Gaussian blurred version. The blurred image is created by a convolution of a five-pixel Gaussian kernel.

A tracking approach is implemented to recreate example trajectories from pixels. At the start, a tube filter extracts points that are part of the high-contrast cell borders. This ensures that only pixels that belong to cell borders are tracked, ignoring noise from cell interiors. The filter is implemented using the eigenvalues of the Hessian matrix.

The highest eigenvalue of the images is then skeletonized using the scipy environment in Python. Randomly chosen points from the skeletonized image of the first frame served as starting points. Using the optical velocity fields, the following location of each pixel is added to the trajectory. The algorithm iterates through the velocity fields and adds the velocities until the accumulated displacement is sufficient to assign the point to a neighboring pixel.

This way, the locations and velocities along a pixel path are gathered. The velocities along the trajectories are used as displacements for calculating mean squared displacement (MSD), as they are not restricted pixel integer values. The MSD is calculated from the list of velocities along a pixel path.

The estimated Cellpose labels are assigned their average optical flow angle for cluster analysis. The gradient is calculated from this image, corresponding to zero inside each label and the angular difference at the border. The borders with more considerable differences than 10° are removed. The remaining regions correspond to ensembles of cells moving together. Mean and standard deviation were determined from independent experiments: WT (m = 20, n = 7), dKD (m = 17, n = 5), co-culture (m = 12, n = 2).

Electric cell-substrate impedance sensing

The monolayer's impedance was measured with an ECIS setup ZΦ (Applied Biophysics, NY, USA). The measurement system consists of an 8-well cell culture dish with gold electrodes deposited on the bottom of each well (8W1E array) attached to a lock-in amplifier with an internal oscillator and relays to switch between the different wells. Each well of the 8-well

electrode array has a small circular working electrode (area: 5 x 10^{-4} cm^2) and a large counter electrode (area: ~ 0.15 cm^2) in coplanar geometry. The small electrode is formed by a circular opening (Ø = 250 µm) in a photoresist layer that insulates the rest of the gold film from the bulk electrolyte. The small electrode size guarantees that the system's overall impedance is represented exclusively by the cells cultured on the small working electrode. Impedance data is obtained by applying an AC signal at a given frequency with 1 V amplitude through a 1 MΩ shunt resistor using the internal oscillator, leading to an approximate current of merely 1 µA running through the cell layer depending on the frequency. The resulting in-phase and out-of-phase voltages across the system are measured by a phase-sensitive lock-in amplifier and converted to the complex impedance of the system.

After adding 200 µL $M10F^-$ to each chamber of an 8W1E array, the array was kept in a humidified incubation chamber (37 °C, 5% CO_2). Cells were passaged as described before and seeded into each chamber (2 x 10^5 cells in 200 µL $M10F^-$). The impedance of cell-covered electrodes was measured using the multiple frequencies over time (MFT) mode at eleven frequencies ranging from 62.5 Hz to 64 kHz with a temporal resolution of approximately 2.6 minutes.

For the second data set (SI Figures 2B, 2C, and 4), 2 x 10^5 (low cell density) and 4 x 10^5 (high density) were seeded in 400 µL $M10F^-$ per chamber. The electrodes were immersed with collagen I rattail (5 µg/cm^2 dissolved in PBS^- with 0.02 M acetic acid), fibronectin (3 µg/cm^2 dissolved in Hank´s Balanced Salt Solution (HBSS)), laminin (2 µg/cm^2 dissolved in HBSS) or poly-L-lysine (4 µg/cm^2 dissolved in distilled water) for 60 minutes at room temperature. The electrodes were then thoroughly rinsed three times with PBS^-. Mean and standard deviation were determined from independent experiments: WT (m = 21, n = 3), dKD (m = 16, n = 2), co-culture (m = 24, n = 3), WT + Blebb (m = 10, n = 2), dKD + Blebb (m = 10, n = 2), WT + CN03 (m = 14, n = 2), dKD + CN03 (m = 14, n = 2). The second data set (SI 1B + 1C) contains measurements of WT low density (m = 11, n = 2), WT high density (m = 11, n = 2), dKD low density (m = 13, n = 2), dKD high density (m = 11, n = 2), 75% WT co-culture (m = 12, n = 2), 50% WT co-culture (m = 12, n = 2) and 25% WT co-culture (m = 10, n = 2).

Micromotion analysis

For recording the micromotion of adherent cells reflecting shape fluctuations comprising predominately cell-substrate distance variation, the complex resistance at a frequency of 4 kHz was recorded.[72] Only confluent layers were considered to rule out cell-number fluctuations on the electrode. Hence, the resistance fluctuations can be assigned to cell shape variations, i.e., cell-substrate distances and the resistance between the cells. A period of 25 hours was selected for the analysis. These trimmed data sets contain both micromotions and an overall trend. To identify the overall trend, we used the empirical mode decomposition method. This signal decomposition yields a frequency-resolved distribution of modes in which the very low-frequency modes display the overall trend. Consequently, subtracting the low-frequency modes from the original signal obtains a detrended signal containing cells' micromotion. Quantitative evaluation of micromotions is performed by determining the variance of these detrended signals (detrended variance analysis, DVA).

Detrended Fluctuation Analysis

DFA analysis, as outlined by Peng et al.,[39] involves the integration and partitioning of datasets of length N into l boxes with a box size of n within each box, a linear trend was subtracted, and the variance F(n) was computed by evaluating the difference between the original data y(k) and the detrended data u(k) using:

$$F(n) = \sqrt{\frac{1}{N}\sum_{k=1}^{N} (y(k) - u(k))^2}.$$

The relationship between F(n) and n was then visualized in a ln(F(n)) - ln(n) plot. The slope of the linear fit applied to this plot provides direct insights into the correlation of the analyzed system. α_{DFA} values and the associated Hurst coefficient H, related to α_{DFA} ($\alpha = H + 1$ for fractional Brownian motion processes), indicate temporal persistence in time series. While for short-range processes, the coupling between successive values decays quickly with distance in an exponential fashion, long-range processes show a power-like decay of the autocorrelation. Mean and standard deviation were determined from independent experiments: WT ($m = 16$, $n = 2$), dKD ($m = 24$, $n = 3$), co-culture ($m = 8$, $n = 1$),

Traction Force Microscopy

For traction force experiments, Petri dishes with beads containing PAA gels were used. 8 x 10^4 cells were seeded on the gel in 300 µL M10F$^-$. After 2 hours of pre-incubation in a humidified incubator (37 °C, 5% CO_2), 2 mL M10F$^-$ were added. For WT-GFP/dKD co-culture measurements, 4 x 10^4 cells of each type were mixed and seeded simultaneously.

Images were acquired using a confocal laser scanning microscope (Fluoview 1200; Olympus, Japan) with a 60x oil immersion objective (UPLFLN 60XOIPH; Olympus, Japan) and a stage top incubation system (blue line; ibidi, Martinsried, Germany) set to 37 °C, 5% CO_2. A phase contrast image of the cells (to determine cell contours using Cellpose) and a fluorescent image of the image plane containing the fluorescent beads were acquired. To remove the cells, a solution of trypsin (2.5%) with 0.05 M EDTA in PBS$^-$ was incubated for 10 to 20 minutes until the cells had completely detached before a second image of the bead-containing plane was acquired. The ImageJ plug-in "Template Matching and Slice Alignment" was used to remove sample shifts during the measurement. The MATLAB application PIVlab was used to calculate the displacement field of the beads.[27] The displacement was determined using four query windows (256 px, 128 px, 64 px, 32 px), and the forces were then calculated from the displacement fields.[69] A mesh size of 16 pixel, a Poisson's ratio of 0.48, and integrated manual noise selection were used. Each gray dot in the plots indicates an independent experiment.

Cell-substrate adhesion measurements

A CellHesion 200 AFM (JPK Instruments; Berlin, Germany) was used to measure cell-substrate adhesion using a tipless cantilever (MLCT-O10, Bruker AFM Probes). To prepare the cantilever, it was first cleaned in acetone for 5 minutes and then exposed to UV light (365 nm) for 15 minutes. This was followed by overnight incubation of the cantilever (at least 12 hours) in 50 µL biotin-BSA solution (0.5 mg/mL in 0.1 M NaHCO3, pH 8.6) at 37 °C. Subsequently, the cantilevers were washed three times with PBS$^-$ and incubated in 50 µL streptavidin solution (0.5 mg/mL in 0.01 M PBS$^-$, pH 7.3) for 20 minutes at room temperature. After 3x PBS$^-$ -wash, a 20 min incubation in concanavalin A-biotin solution (0.2 mg/mL in PBS$^-$) was performed to attach cells firmly to the cantilever. The whole procedure was adopted from Wojcikiewicz et al.[73] 6 x 10^4 cells suspended in M10F$^-$ medium (containing HEPES and penicillin-streptomycin) were added to a PAA gel for adhesion measurements. To attach a cell to the cantilever, a pre-adhered cell was picked with a setpoint of 2 nN and allowed to adhere to the cantilever for 15 minutes without contact with the PAA gel. Subsequently, the cell was pressed onto the substrate

with a setpoint of 2 nN for 150 seconds. The approach and retract velocity were set to 0.5 µm s^{-1}. The maximal adhesion force was determined using JPK Data Processing software after linear baseline correction and detection of the contact time point. Mean and standard deviation were determined from independent experiments: WT (m = 25, n = 6), dKD (m = 34, n = 6), WT + Blebb (m = 70, n = 4), dKD + Blebb (m = 45, n = 4).

Centrifugation assay

The centrifugation assay was performed as described elsewhere.[42,43] 1 x 10^5 Cells were seeded on top of a coverslip (13 mm diameter), which was placed in a self-built holder. The sample was placed in a centrifuge (Megafuge 16R Centrifuge, Thermo Electron LED GmbH, Langenselbold, Germany) after the desired incubation time. An angular velocity of 5000 rotations/min and a duration of 5 min were selected. The whole area of the coverslip was imaged before and after the centrifugation with an inverted optical microscope (BZ-X810; Keyence, Neu-Isenburg, Germany) equipped with a 10× phase-contrast objective (Plan Fluor 10x; Nikon Europe B.V., Amstelveen, The Netherlands). Mean and standard deviation were determined from independent experiments: WT (m = 3, n = 3), dKD (m = 3, n = 3).

Metal-induced energy transfer

All MIET measurements were carried out with a custom-built confocal microscope equipped with a multichannel picosecond event timer (HydraHarp 400, PicoQuant GmbH; Berlin, Germany), allowing for fluorescence lifetime imaging. The system was equipped with a high numerical aperture objective (Apo N, 60×/1.49 NA oil immersion, Olympus) for both focusing excitation light and collecting fluorescence light. A white-light laser system (SC400-4-20, Fianium) with an acoustic-optical tunable filter (AOTFnC-400.650-TN, AA Optic) served as the excitation source (λ_{exc} = 645 nm). The excitation light was reflected by a non-polarizing beam splitter towards the objective. Back-scattered excitation light was blocked with a long-pass filter (BLP01-635R, Semrock). Collected fluorescence was focused onto the active area of an avalanche photodiode (PDM series, MPD). The fluorescence decay curves were fitted with a multi-exponential decay model (up to 10 mono-exponential components), from which the average excited state lifetime was calculated. A semitransparent metallic film consists of a 15 nm gold film deposited on a 2 nm titanium film for better adhesion to glass. The metal films were prepared by vapor deposition onto a glass bottom Petri dish (µ-Dish, Ibidi) using an electron beam source (Univex 400, Leybold, Cologne, Germany) under high-vacuum conditions (~10^{-6} mbar). During vapor deposition, the film thickness was monitored using an oscillating quartz unit and verified using a profilometer. 5 x 10^5 cells were seeded on the inner surface of the petri dish, as described above. After approximately 24 hours in the incubator (37 °C and 5% CO_2), the cells were washed three times with $M10F^-$. A solution of 1 µL CellMask Plasma Membrane Stain Deep Red with 499 µL $M10F^-$ was added to the cells. After ten minutes of incubation (37 °C and 5% CO_2), cells were washed three times with $M10F^-$ and fixed in a 4% paraformaldehyde solution for 15 min. Cells were stored in PBS^- for measurement. The analysis of the raw data was performed with a self-written Matlab script described in Karedla et al.[70,74] Cell center elevations were quantified by manually cropping the elevation profiles and determining a mean value. Mean and standard deviation were determined from independent experiments: WT (m = 6, n = 2), dKD (m = 8, n = 2), WT + Blebb (m = 6, n = 1), dKD + Blebb (m = 5, n = 1), WT + CN03 (m = 6, n = 1), dKD + CN03 (m = 7, n = 1).

Drug Treatment

Para-amino-blebbistatin (Blebb) was dissolved at 50 mM in DMSO, and the aliquots were stored at -20 °C. Cell samples were washed twice with $M10F^-$ and incubated with $M10F^-$ containing 50 µM of Blebb at 37 °C and 5% CO_2 for 30 min. Afterward, three washes with $M10F^-$ were performed, and the samples were prepared for the respective experiments.

A stock solution of Rho Activator II (CN03) was prepared at 0.1g/L in water and stored at -70 °C. After washing once with $M10F^-$, the cells were incubated with 1 µg/mL CN03 (in MEM) at 37 °C and 5% CO_2 for 3.5 h. Subsequently, the samples were washed three times with $M10F^-$ and prepared for further experiments.

A stock solution of Mitomycin C (MitoC) was prepared in water (500 µg/mL) and stored in aliquots of 150 µL at -20 °C. Samples were seeded as before and treated with 10 µg/mL MitoC in an incubator at 37 °C, 5% CO_2 for 1 hour. The samples were washed three times with $M10F^-$ and used for subsequent experiments.

Staining

Cells were seeded on the PAA gels as described above. After 24h, samples were washed three times with PBS and then incubated for 15 min in PFA (4% (w/v) in PBS^-) to fixate cells. Then, permeabilization was performed with Triton X-100 (0.1% (v/v) in PBS^-) for 15 minutes. After three subsequent washes with PBS^- blocking/dilution buffer (PBS^- containing 2% (v/v) Normal Goat Serum) was added for 30 minutes.

Samples were incubated with a primary antibody (Phospho-myosin: 2 µg mL-1 (1:50 (v/v)) light chain 2 (Ser 19) rabbit IgG1) diluted in blocking/dilution buffer for 1 hour. After incubation with the primary antibody, the samples were briefly rinsed with PBS^- before washing three times with PBS^- (each 5min on a shaker plate). Then, the secondary labeling solution (in blocking/dilution buffer) with the second antibody (1:1000 (v/v) AlexaFluor 488-conjugated goat anti-rabbit IgG H&L) and AlexaFluor 546-phalloidin (165 nM) was incubated with the sample for one h. Samples were washed three times with PBS^- (each 5min on a shaker plate) and kept in PBS^- for imaging.

Intensity quantification

Images of the basal side were taken on the confocal laser scanning microscope (Fluoview 1200, Olympus, Japan). Myosin staining was imaged with a 60x oil immersion objective (UPLFLN 60XOIPH, NA1.25, Olympus, Japan) and actin staining with a 100x oil immersion objective (UPLXAPO 100x/NA1.45, Olympus). Data sets were created on the same day with the same settings. Myosin intensity was measured in the cell center. For this, the corresponding phase contrast images were segmented by Cellpose to create a mask of the cell borders. ImageJ was subsequently used to analyze the corresponding intensities. Actin intensity measurements were analyzed by ImageJ averaged over an entire image. Mean and standard deviation were determined from independent experiments: WT myosin ($m = 4$, $n = 1$), dKD myosin ($m = 3$, $n = 1$), WT actin ($m = 17$, $n = 2$), dKD actin ($m = 16$, $n = 2$), WT actin + CN03 ($m = 16$, $n = 1$), dKD actin + CN03 ($m = 16$, $n = 1$).

Quantification and statistical analysis

All data were written in the text as mean ± standard deviation. The gray dots in the box plots represent independent experiments (biological and technical replicates). Box plots show the median with the 25th and 75th percentiles, and whiskers show the 5th and 95th percentiles. A significance test (Wilcoxon rank-sum test) was performed for all data sets, denoted by the *p*-

value. A p-value of < 0.1 was considered significant and denoted by one asterisk (*). $p < 0.05$ and $p < 0.005$ were indicated by two (**) and three (***) asterisks, respectively. The number of biological replicates (n) and technical replicates (m) of the experiments is given in the respective method sections.

References

1. Friedl, P., and Gilmour, D. (2009). Collective cell migration in morphogenesis, regeneration and cancer. Nat Rev Mol Cell Biol *10*, 445–457. 10.1038/nrm2720.

2. Rørth, P. (2009). Collective Cell Migration. Annual Review of Cell and Developmental Biology *25*, 407–429. 10.1146/annurev.cellbio.042308.113231.

3. Trepat, X., and Sahai, E. (2018). Mesoscale physical principles of collective cell organization. Nature Phys *14*, 671–682. 10.1038/s41567-018-0194-9.

4. Mayor, R., and Etienne-Manneville, S. (2016). The front and rear of collective cell migration. Nat Rev Mol Cell Biol *17*, 97–109. 10.1038/nrm.2015.14.

5. Campanale, J.P., and Montell, D.J. (2023). Who's really in charge: Diverse follower cell behaviors in collective cell migration. Current Opinion in Cell Biology *81*, 102160. 10.1016/j.ceb.2023.102160.

6. Lim, S.E., Vicente-Munuera, P., and Mao, Y. (2024). Forced back into shape: Mechanics of epithelial wound repair. Current Opinion in Cell Biology *87*, 102324. 10.1016/j.ceb.2024.102324.

7. Gonzalez-Rodriguez, D., Guevorkian, K., Douezan, S., and Brochard-Wyart, F. (2012). Soft Matter Models of Developing Tissues and Tumors. Science *338*, 910–917. 10.1126/science.1226418.

8. Jülicher, F., and Eaton, S. (2017). Emergence of tissue shape changes from collective cell behaviours. Seminars in Cell & Developmental Biology *67*, 103–112. 10.1016/j.semcdb.2017.04.004.

9. Alert, R., and Trepat, X. (2020). Physical Models of Collective Cell Migration. Annual Review of Condensed Matter Physics *11*, 77–101. 10.1146/annurev-conmatphys-031218-013516.

10. Saraswathibhatla, A., and Notbohm, J. (2020). Tractions and Stress Fibers Control Cell Shape and Rearrangements in Collective Cell Migration. Phys. Rev. X *10*, 011016. 10.1103/PhysRevX.10.011016.

11. Pérez-González, C., Alert, R., Blanch-Mercader, C., Gómez-González, M., Kolodziej, T., Bazellieres, E., Casademunt, J., and Trepat, X. (2019). Active wetting of epithelial tissues. Nature Phys *15*, 79–88. 10.1038/s41567-018-0279-5.

12. Legerstee, K., Geverts, B., Slotman, J.A., and Houtsmuller, A.B. (2019). Dynamics and distribution of paxillin, vinculin, zyxin and VASP depend on focal adhesion location and orientation. Sci Rep *9*, 10460. 10.1038/s41598-019-46905-2.

13. Kim, D., and Wirtz, D. (2013). Focal adhesion size uniquely predicts cell migration. FASEB j. *27*, 1351–1361. 10.1096/fj.12-220160.

14. Han, S.J., Bielawski, K.S., Ting, L.H., Rodriguez, M.L., and Sniadecki, N.J. (2012). Decoupling Substrate Stiffness, Spread Area, and Micropost Density: A Close Spatial Relationship between Traction Forces and Focal Adhesions. Biophysical Journal *103*, 640–648. 10.1016/j.bpj.2012.07.023.

15. Citi, S. (2019). The mechanobiology of tight junctions. Biophys Rev *11*, 783–793. 10.1007/s12551-019-00582-7.

16. Hatte, G., Prigent, C., and Tassan, J.-P. (2017). Tight junctions negatively regulate mechanical forces applied to adherens junctions in vertebrate epithelial tissue. Journal of Cell Science, jcs.208736. 10.1242/jcs.208736.

17. Bazellières, E., Conte, V., Elosegui-Artola, A., Serra-Picamal, X., Bintanel-Morcillo, M., Roca-Cusachs, P., Muñoz, J.J., Sales-Pardo, M., Guimerà, R., and Trepat, X. (2015). Control of cell–cell forces and collective cell dynamics by the intercellular adhesome. *17*.

18. Du, D., Xu, F., Yu, L., Zhang, C., Lu, X., Yuan, H., Huang, Q., Zhang, F., Bao, H., Jia, L., et al. (2010). The Tight Junction Protein, Occludin, Regulates the Directional Migration of Epithelial Cells. Developmental Cell *18*, 52–63. 10.1016/j.devcel.2009.12.008.

19. Fanning, A.S., Van Itallie, C.M., and Anderson, J.M. (2012). Zonula occludens-1 and -2 regulate apical cell structure and the zonula adherens cytoskeleton in polarized epithelia. MBoC *23*, 577–590. 10.1091/mbc.e11-09-0791.

20. Cartagena-Rivera, A.X., Van Itallie, C.M., Anderson, J.M., and Chadwick, R.S. (2017). Apical surface supracellular mechanical properties in polarized epithelium using noninvasive acoustic force spectroscopy. Nat Commun *8*, 1030. 10.1038/s41467-017-01145-8.

21. Choi, W., Acharya, B.R., Peyret, G., Fardin, M.-A., Mège, R.-M., Ladoux, B., Yap, A.S., Fanning, A.S., and Peifer, M. (2016). Remodeling the zonula adherens in response to tension and the role of afadin in this response. Journal of Cell Biology *213*, 243–260. 10.1083/jcb.201506115.

22. Skamrahl, M., Pang, H., Ferle, M., Gottwald, J., Rübeling, A., Maraspini, R., Honigmann, A., Oswald, T.A., and Janshoff, A. (2021). Tight Junction ZO Proteins Maintain Tissue Fluidity, Ensuring Efficient Collective Cell Migration. Advanced Science *8*, 2100478. 10.1002/advs.202100478.

23. Nietmann, P., Bodenschatz, J.E.F., Cordes, A.M., Gottwald, J., Rother-Nöding, H., Oswald, T., and Janshoff, A. (2022). Epithelial cells fluidize upon adhesion but display mechanical homeostasis in the adherent state. Biophysical Journal *121*, 361–373. 10.1016/j.bpj.2021.12.042.

24. Raya-Sandino, A., Castillo-Kauil, A., Domínguez-Calderón, A., Alarcón, L., Flores-Benitez, D., Cuellar-Perez, F., López-Bayghen, B., Chávez-Munguía, B., Vázquez-Prado, J., and González-Mariscal, L. (2017). Zonula occludens-2 regulates Rho proteins activity and the development of epithelial cytoarchitecture and barrier function. Biochimica et Biophysica Acta (BBA) - Molecular Cell Research *1864*, 1714–1733. 10.1016/j.bbamcr.2017.05.016.

25. Tornavaca, O., Chia, M., Dufton, N., Almagro, L.O., Conway, D.E., Randi, A.M., Schwartz, M.A., Matter, K., and Balda, M.S. (2015). ZO-1 controls endothelial adherens junctions, cell–cell tension, angiogenesis, and barrier formation. Journal of Cell Biology *208*, 821–838. 10.1083/jcb.201404140.

26. Skamrahl, M., Schünemann, J., Mukenhirn, M., Pang, H., Gottwald, J., Jipp, M., Ferle, M., Rübeling, A., Oswald, T.A., Honigmann, A., et al. (2023). Cellular segregation in cocultures is driven by differential adhesion and contractility on distinct timescales. Proceedings of the National Academy of Sciences *120*, e2213186120. 10.1073/pnas.2213186120.

27. Thielicke, W., and Sonntag, R. (2021). Particle Image Velocimetry for MATLAB: Accuracy and enhanced algorithms in PIVlab. *9*, 12. 10.5334/jors.334.

28. Zimmermann, J., Camley, B.A., Rappel, W.-J., and Levine, H. (2016). Contact inhibition of locomotion determines cell–cell and cell–substrate forces in tissues. Proceedings of the National Academy of Sciences *113*, 2660–2665. 10.1073/pnas.1522330113.

29. Abercrombie, M., and Heaysman, J.E.M. (1954). Observations on the social behaviour of cells in tissue culture: II. “Monolayering” of fibroblasts. Experimental Cell Research *6*, 293–306. 10.1016/0014-4827(54)90176-7.

30. Stringer, C., Wang, T., Michaelos, M., and Pachitariu, M. (2021). Cellpose: a generalist algorithm for cellular segmentation. Nat Methods *18*, 100–106. 10.1038/s41592-020-01018-x.

31. Petitjean, L., Reffay, M., Grasland-Mongrain, E., Poujade, M., Ladoux, B., Buguin, A., and Silberzan, P. (2010). Velocity Fields in a Collectively Migrating Epithelium. Biophysical Journal *98*, 1790–1800. 10.1016/j.bpj.2010.01.030.

32. Merkel, M., and Manning, M.L. (2018). A geometrically controlled rigidity transition in a model for confluent 3D tissues. New J. Phys. *20*, 022002. 10.1088/1367-2630/aaaa13.

33. Giaever, I., and Keese, C.R. (1991). Micromotion of mammalian cells measured electrically. Cell Biology.

34. Tarantola, M., Pietuch, A., Schneider, D., Rother, J., Sunnick, E., Rosman, C., Pierrat, S., Sönnichsen, C., Wegener, J., and Janshoff, A. (2011). Toxicity of gold-nanoparticles: Synergistic effects of shape and surface functionalization on micromotility of epithelial cells. Nanotoxicology *5*, 254–268. 10.3109/17435390.2010.528847.

35. Tung, T.-H., Wang, S.-H., Huang, C.-C., Su, T.-Y., and Lo, C.-M. (2020). Use of Discrete Wavelet Transform to Assess Impedance Fluctuations Obtained from Cellular Micromotion. Sensors *20*, 3250. 10.3390/s20113250.

36. Huang, N.E., Shen, Z., Long, S.R., Wu, M.C., Shih, H.H., Zheng, Q., Yen, N.-C., Tung, C.C., and Liu, H.H. (1998). The empirical mode decomposition and the Hilbert spectrum for nonlinear and non-stationary time series analysis. Proceedings of the Royal Society of London. Series A: Mathematical, Physical and Engineering Sciences *454*, 903–995. 10.1098/rspa.1998.0193.

37. Quinn, A., Lopes-dos-Santos, V., Dupret, D., Nobre, A., and Woolrich, M. (2021). EMD: Empirical Mode Decomposition and Hilbert-Huang Spectral Analyses in Python. JOSS *6*, 2977. 10.21105/joss.02977.

38. Huang, N.E., Hu, K., Yang, A.C.C., Chang, H.-C., Jia, D., Liang, W.-K., Yeh, J.R., Kao, C.-L., Juan, C.-H., Peng, C.K., et al. (2016). On Holo-Hilbert spectral analysis: a full informational spectral representation for nonlinear and non-stationary data. Philosophical Transactions of the Royal Society A: Mathematical, Physical and Engineering Sciences *374*, 20150206. 10.1098/rsta.2015.0206.

39. Peng, C.-K., Havlin, S., Stanley, H.E., and Goldberger, A.L. (1995). Quantification of scaling exponents and crossover phenomena in nonstationary heartbeat time series. Chaos: An Interdisciplinary Journal of Nonlinear Science *5*, 82–87. 10.1063/1.166141.

40. Gauquelin, E., Tlili, S., Gay, C., Peyret, G., Mège, R.-M., A. Fardin, M., and Ladoux, B. (2019). Influence of proliferation on the motions of epithelial monolayers invading adherent strips. Soft Matter *15*, 2798–2810. 10.1039/C9SM00105K.

41. Tlili, S., Gauquelin, E., Li, B., Cardoso, O., Ladoux, B., Delanoë-Ayari, H., and Graner, F. (2018). Collective cell migration without proliferation: density determines cell velocity and wave velocity. Royal Society Open Science *5*, 172421. 10.1098/rsos.172421.

42. Reyes, C.D., and García, A.J. (2003). A centrifugation cell adhesion assay for high-throughput screening of biomaterial surfaces. J Biomedical Materials Res *67A*, 328–333. 10.1002/jbm.a.10122.

43. Christ, K.V., and Turner, K.T. (2010). Methods to Measure the Strength of Cell Adhesion to Substrates. Journal of Adhesion Science and Technology *24*, 2027–2058. 10.1163/016942410X507911.

44. Hennig, K., Wang, I., Moreau, P., Valon, L., DeBeco, S., Coppey, M., Miroshnikova, Y.A., Albiges-Rizo, C., Favard, C., Voituriez, R., et al. (2020). Stick-slip dynamics of cell adhesion triggers spontaneous symmetry breaking and directional migration of mesenchymal cells on one-dimensional lines. Sci. Adv. *6*, eaau5670. 10.1126/sciadv.aau5670.

45. Meili, R., Alonso-Latorre, B., del Álamo, J.C., Firtel, R.A., and Lasheras, J.C. (2010). Myosin II Is Essential for the Spatiotemporal Organization of Traction Forces during Cell Motility. MBoC *21*, 405–417. 10.1091/mbc.e09-08-0703.

46. Zancla, A., Mozetic, P., Orsini, M., Forte, G., and Rainer, A. (2022). A primer to traction force microscopy. Journal of Biological Chemistry *298*, 101867. 10.1016/j.jbc.2022.101867.

47. Chizhik, A.I., Rother, J., Gregor, I., Janshoff, A., and Enderlein, J. (2014). Metal-induced energy transfer for live cell nanoscopy. Nature Photon *8*, 124–127. 10.1038/nphoton.2013.345.

48. Berndt, M., Lorenz, M., Enderlein, J., and Diez, S. (2010). Axial Nanometer Distances Measured by Fluorescence Lifetime Imaging Microscopy. Nano Lett. *10*, 1497–1500. 10.1021/nl100593x.

49. Baronsky, T., Ruhlandt, D., Brückner, B.R., Schäfer, J., Karedla, N., Isbaner, S., Hähnel, D., Gregor, I., Enderlein, J., Janshoff, A., et al. (2017). Cell–Substrate Dynamics of the Epithelial-to-Mesenchymal Transition. Nano Lett. *17*, 3320–3326. 10.1021/acs.nanolett.7b01558.

50. Chizhik, A.M., Wollnik, C., Ruhlandt, D., Karedla, N., Chizhik, A.I., Hauke, L., Hähnel, D., Gregor, I., Enderlein, J., and Rehfeldt, F. (2018). Dual-color metal-induced and Förster resonance energy transfer for cell nanoscopy. MBoC *29*, 846–851. 10.1091/mbc.E17-05-0314.

51. Gregor, I., Chizhik, A., Karedla, N., and Enderlein, J. (2019). Metal-induced energy transfer. Nanophotonics *8*, 1689–1699. 10.1515/nanoph-2019-0201.

52. Várkuti, B.H., Képiró, M., Horváth, I.Á., Végner, L., Ráti, S., Zsigmond, Á., Hegyi, G., Lenkei, Z., Varga, M., and Málnási-Csizmadia, A. (2016). A highly soluble, non-phototoxic, non-fluorescent blebbistatin derivative. Sci Rep *6*, 26141. 10.1038/srep26141.

53. Angelini, T.E., Hannezo, E., Trepat, X., Marquez, M., Fredberg, J.J., and Weitz, D.A. (2011). Glass-like dynamics of collective cell migration. Proceedings of the National Academy of Sciences *108*, 4714–4719. 10.1073/pnas.1010059108.

54. Nnetu, K.D., Knorr, M., Pawlizak, S., Fuhs, T., and Käs, J.A. (2013). Slow and anomalous dynamics of an MCF-10A epithelial cell monolayer. Soft Matter *9*, 9335–9341. 10.1039/C3SM50806D.

55. Garcia, S., Hannezo, E., Elgeti, J., Joanny, J.-F., Silberzan, P., and Gov, N.S. (2015). Physics of active jamming during collective cellular motion in a monolayer. Proceedings of the National Academy of Sciences *112*, 15314–15319. 10.1073/pnas.1510973112.

56. Park, J.-A., Kim, J.H., Bi, D., Mitchel, J.A., Qazvini, N.T., Tantisira, K., Park, C.Y., McGill, M., Kim, S.-H., Gweon, B., et al. (2015). Unjamming and cell shape in the asthmatic airway epithelium. Nature Mater *14*, 1040–1048. 10.1038/nmat4357.

57. Capaldo, C.T., Koch, S., Kwon, M., Laur, O., Parkos, C.A., and Nusrat, A. (2011). Tight function zonula occludens-3 regulates cyclin D1–dependent cell proliferation. MBoC *22*, 1677–1685. 10.1091/mbc.e10-08-0677.

58. Sourisseau, T., Georgiadis, A., Tsapara, A., Ali, R.R., Pestell, R., Matter, K., and Balda, M.S. (2006). Regulation of PCNA and Cyclin D1 Expression and Epithelial Morphogenesis by the ZO-1-Regulated Transcription Factor ZONAB/DbpA. Molecular and Cellular Biology *26*, 2387–2398. 10.1128/MCB.26.6.2387-2398.2006.

59. Różycki, B., Weikl, T.R., and Lipowsky, R. (2007). Stochastic resonance for adhesion of membranes with active stickers. Eur. Phys. J. E *22*, 97–106. 10.1140/epje/i2006-10075-3.

60. Sabass, B., and Schwarz, U.S. (2010). Modeling cytoskeletal flow over adhesion sites: competition between stochastic bond dynamics and intracellular relaxation. J. Phys.: Condens. Matter *22*, 194112. 10.1088/0953-8984/22/19/194112.

61. Schneider, D., Tarantola, M., and Janshoff, A. (2011). Dynamics of TGF-β induced epithelial-to-mesenchymal transition monitored by Electric Cell-Substrate Impedance Sensing. Biochimica et Biophysica Acta (BBA) - Molecular Cell Research *1813*, 2099–2107. 10.1016/j.bbamcr.2011.07.016.

62. Schneider, D., and Janshoff, A. (2012). Inhibition of actin dynamics during epithelial-to-mesenchymal transition. Biochemical and Biophysical Research Communications *419*, 221–225. 10.1016/j.bbrc.2012.01.151.

63. Aguilar-Cuenca, R., Juanes-García, A., and Vicente-Manzanares, M. (2014). Myosin II in mechanotransduction: master and commander of cell migration, morphogenesis, and cancer. Cell. Mol. Life Sci. *71*, 479–492. 10.1007/s00018-013-1439-5.

64. Tambe, D.T., Corey Hardin, C., Angelini, T.E., Rajendran, K., Park, C.Y., Serra-Picamal, X., Zhou, E.H., Zaman, M.H., Butler, J.P., Weitz, D.A., et al. (2011). Collective cell guidance by cooperative intercellular forces. Nature Mater *10*, 469–475. 10.1038/nmat3025.

65. Ng, M.R., Besser, A., Brugge, J.S., and Danuser, G. (2014). Mapping the dynamics of force transduction at cell–cell junctions of epithelial clusters. eLife *3*, e03282. 10.7554/eLife.03282.

66. Arzash, S., Tah, I., Liu, A.J., and Manning, M.L. (2024). Tuning for fluidity using fluctuations in biological tissue models. Preprint at arXiv, 10.48550/arXiv.2312.11683 10.48550/arXiv.2312.11683.

67. Yanagida, A., Corujo-Simon, E., Revell, C.K., Sahu, P., Stirparo, G.G., Aspalter, I.M., Winkel, A.K., Peters, R., Belly, H.D., Cassani, D.A.D., et al. (2022). Cell surface fluctuations regulate early embryonic lineage sorting. Cell *185*, 777-793.e20. 10.1016/j.cell.2022.01.022.

68. Beutel, O., Maraspini, R., Pombo-García, K., Martin-Lemaitre, C., and Honigmann, A. (2019). Phase Separation of Zonula Occludens Proteins Drives Formation of Tight Junctions. Cell *179*, 923-936.e11. 10.1016/j.cell.2019.10.011.

69. Huang, Y., Schell, C., Huber, T.B., Şimşek, A.N., Hersch, N., Merkel, R., Gompper, G., and Sabass, B. (2019). Traction force microscopy with optimized regularization and automated Bayesian parameter selection for comparing cells. Sci Rep *9*, 539. 10.1038/s41598-018-36896-x.

70. Ghosh, A., Chizhik, A.I., Karedla, N., and Enderlein, J. (2021). Graphene- and metal-induced energy transfer for single-molecule imaging and live-cell nanoscopy with (sub)-nanometer axial resolution. Nat Protoc *16*, 3695–3715. 10.1038/s41596-021-00558-6.

71. Farnebäck, G. (2003). Two-Frame Motion Estimation Based on Polynomial Expansion. In Image Analysis Lecture Notes in Computer Science., J. Bigun and T. Gustavsson, eds. (Springer), pp. 363–370. 10.1007/3-540-45103-X_50.

72. Lo, C.-M., Keese, C.R., and Giaever, I. (1993). Monitoring Motion of Confluent Cells in Tissue Culture. Experimental Cell Research *204*, 102–109. 10.1006/excr.1993.1014.

73. Wojcikiewicz, E.P., Zhang, X., and Moy, V.T. (2004). Force and compliance measurements on living cells using atomic force microscopy (AFM). Biol. Proced. Online *6*, 1–9. 10.1251/bpo67.

74. Karedla, N., Chizhik, A.M., Stein, S.C., Ruhlandt, D., Gregor, I., Chizhik, A.I., and Enderlein, J. (2018). Three-dimensional single-molecule localization with nanometer accuracy using Metal-Induced Energy Transfer (MIET) imaging. The Journal of Chemical Physics *148*, 204201. 10.1063/1.5027074.

Figures

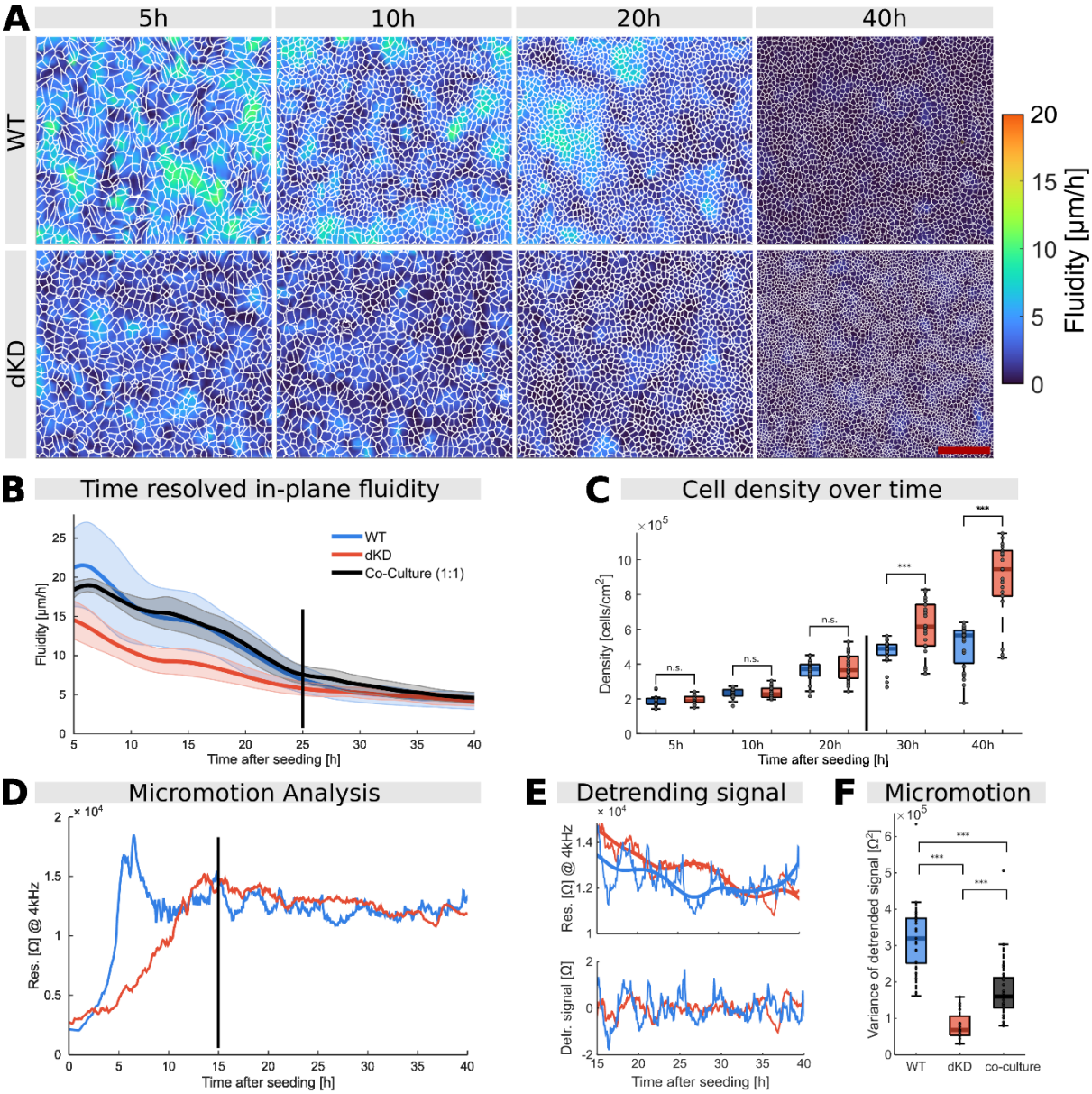

Figure 1. 3D Motility is altered in tight junction deficient epithelia. A) Representative in-plane fluidity maps generated from the corresponding velocity vectors obtained from PIV with cell outlines (white) obtained from Cellpose cell segmentation starting from the point of confluence (5 h) until 40 h after the experiment started. Scale bar: 160 µm. B) Corresponding averaged time-resolved in-plane fluidity showing a "baseline fluidity" being reached for all samples after approx. 25 h (black line). C) Cell densities per cm^2 obtained from Cellpose cell segmentation. The black line between 20 h and 30 h indicates reaching "baseline fluidity." D) Representative resistance fluctuations of WT and dKD cell monolayers measured with a frequency at 4 kHz. After the point of confluency (black line) micromotions, i.e., cell-substrate-fluctuations of the cells, were analyzed. Note: The timeline between B and D is not comparable due to differences in seeding and substrates used. E) Detrending of the signal using the empirical mode decomposition (EMD) method. Top: Trimmed data from D and overall trend (thicker lines). Bottom: Detrended signals after subtraction of the low-frequency overall trend. F) Detrended variance analysis.

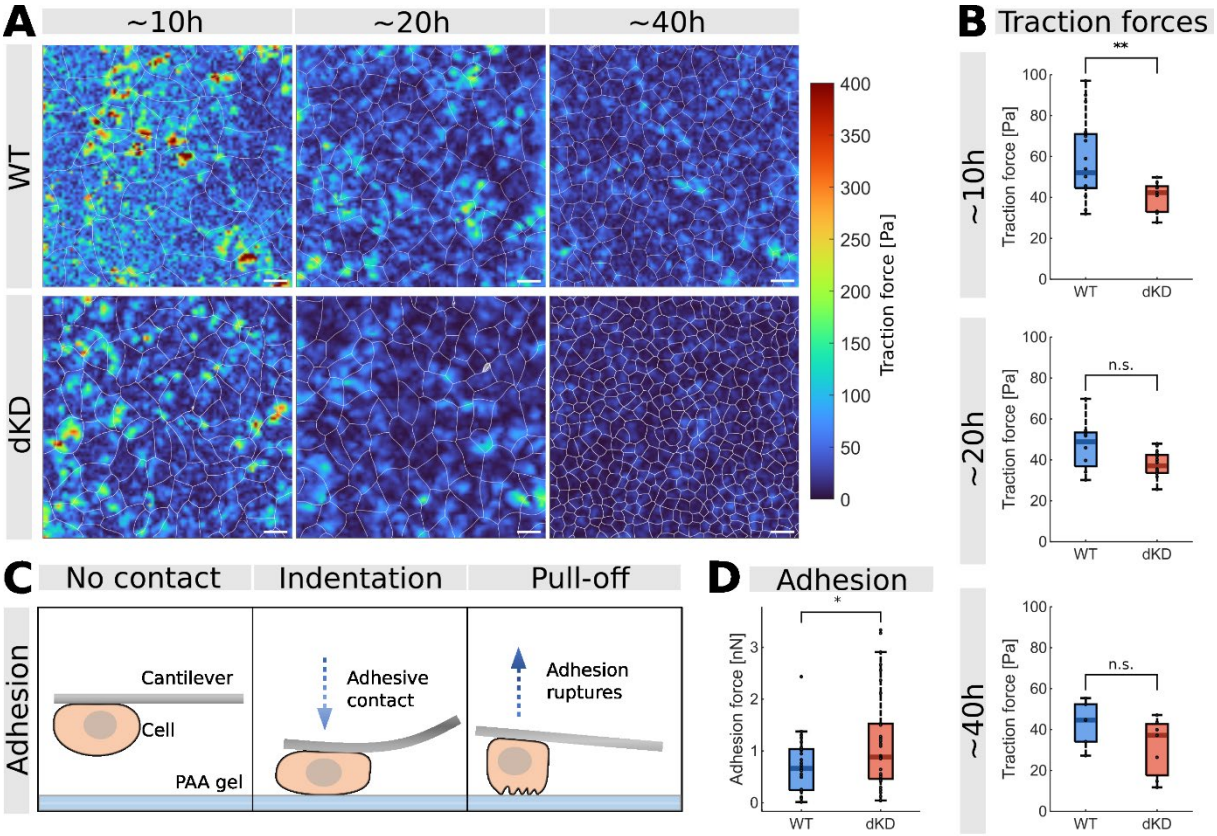

Figure 2: Traction forces decrease, while adhesion increases in ZO1/ZO2 impaired cells. A) Representative traction force maps of WT and dKD cell monolayers with cell outlines (white) obtained from Cellpose cell segmentation. Scale bars: 20µm. B) Average traction forces of the cell monolayers at the three different time points shown in A). C) AFM-based measurement of cell-substrate adhesions. The cell attached to the cantilever is brought in contact with a polyacrylamide (PAA) gel for 150 s. Afterward, adhesion can be measured by disengaging the cell from the gel. D) Average cell-substrate adhesions (max. adhesion force) on a 1.6 kPa stiff PAA gel.

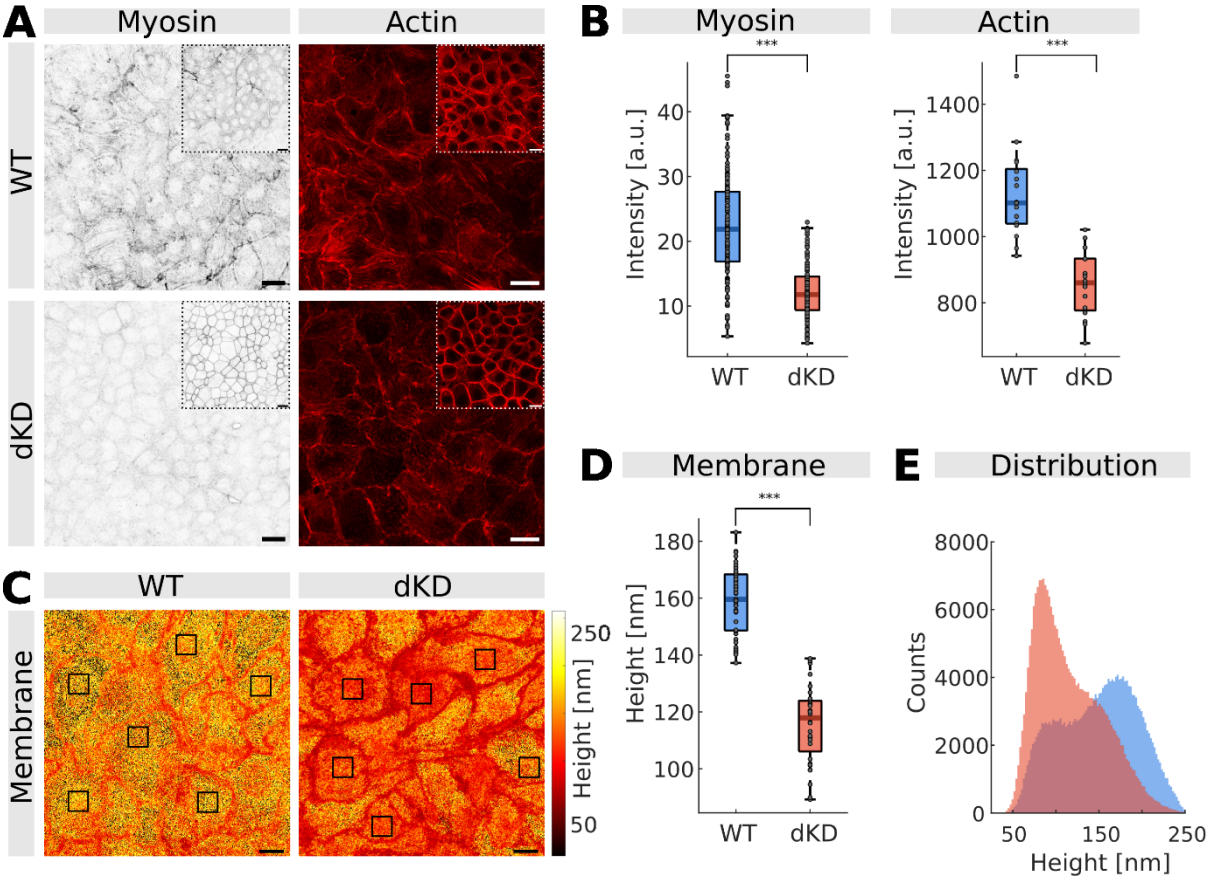

Figure 3. Contractility gradient in tight junction KO cells. A) Representative fluorescence images of WT and dKD cell monolayers seeded on PAA gels (basal side, inverse contrast). Actin is stained with Phalloidin-AF-546 (red), while myosin II is immunostained with AF488 (p-myosin-2 antibody). The upper corners show the corresponding images of the apical side. Scale bar: 15 µm. B) Fluorescence intensities of stained myosin and actin, respectively. C) Representative height (distance between the surface and basal membrane) maps obtained from MIET microscopy. For further analysis, areas in cell centers were selected (black rectangles), and the corresponding analysis is shown in D). Scale bar: 20 µm. E) Representative height distributions of a confluent cell layer (100 µm x 100 µm).

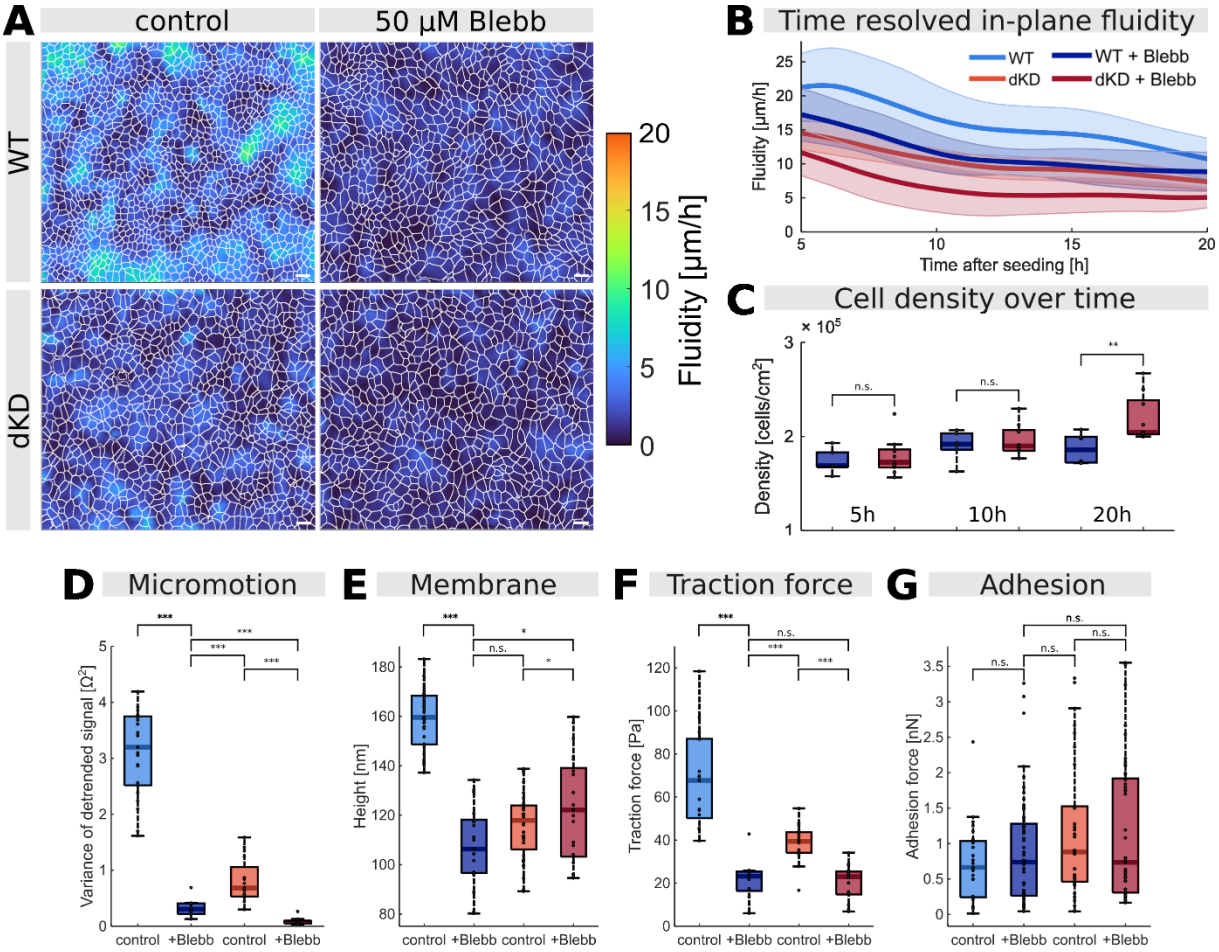

Figure 4. Impact of myosin II on cellular motility. A) Representative in-plane fluidity maps generated from the corresponding velocity vectors obtained from PIV with cell outlines obtained from Cellpose cell segmentation overlayed in white. Scale bars: 40 µm. B) In-plane fluidity measurements of WT and dKD monolayers treated with 50 µM Blebb compared with untreated monolayers. C) Cell densities obtained from Cellpose cell segmentation. D) Detrended variance analysis of micromotions measured with ECIS. E) Average height values of the basal membrane from the surface calculated from selected cell centers of MIET microscopy images. F) Average traction forces of confluent cell monolayers between 10 h and 20 h after seeding. G) Average cell-substrate adhesion forces (max. value) measured by AFM.

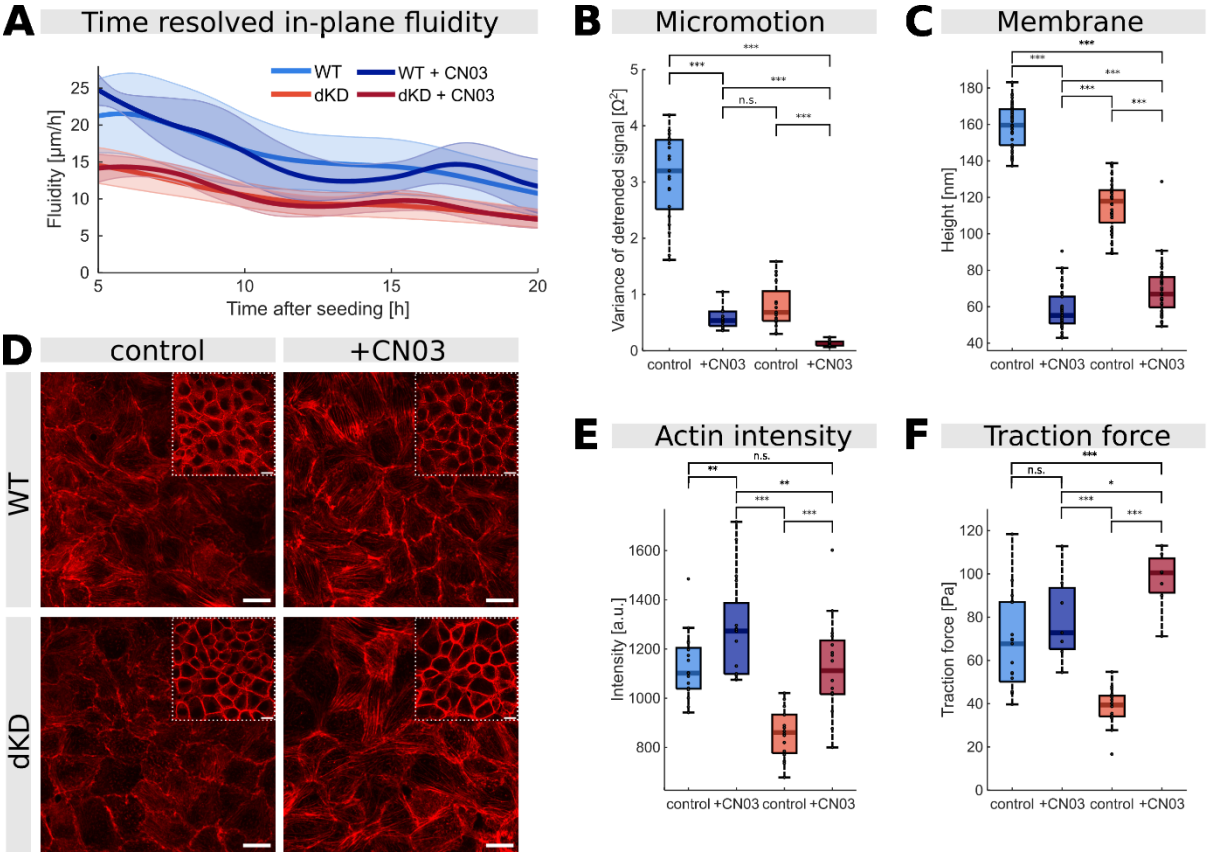

Figure 5. Impact of rho activation on cellular motility. A) In-plane fluidity measurements of WT and dKD monolayers treated with 1 µg/mL of rho activator CN03 compared with untreated monolayers. B) Detrended variance analysis of micromotions (cell-substrate-fluctuations) measured with ECIS. C) Average height values of the basal membrane from the surface calculated from selected cell centers of MIET microscopy images. D) Representative fluorescence images of WT and dKD cell monolayers seeded on PAA gels (basal side). Actin is stained with phalloidin-AF-546 (red). The upper corners show the corresponding images of the apical side. Scale bars: 15 µm. E) Fluorescence intensities of actin. F) Average traction forces of confluent cell monolayer between 10 h and 20 h after seeding.

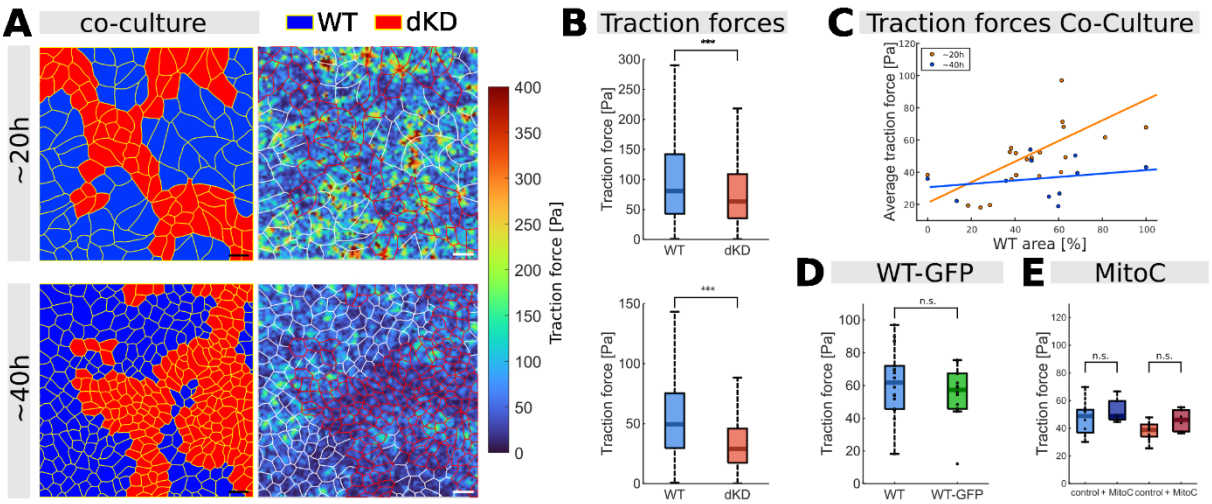

Figure 6. Average traction forces of co-culture. A) Representative traction force maps (right images) of co-culture monolayers. The left images display the distribution of WT and dKD cells within the monolayer. Cell outlines obtained from Cellpose cell segmentation are overlayed in white/red in both images. Scale bar: 20 µm. B) Average traction forces for WT and dKD cells within the co-culture monolayer 20 hours (upper plot) and 40 hours (lower plot) after seeding corresponding to the time points shown in A). C) Average traction forces of co-cultures with different WT/dKD ratios. The lines are drawn for better visibility. D) Average traction forces of WT and WT-GFP monolayers. E) Average traction forces for WT and dKD monolayers treated with Mitomycin C to inhibit cell division.

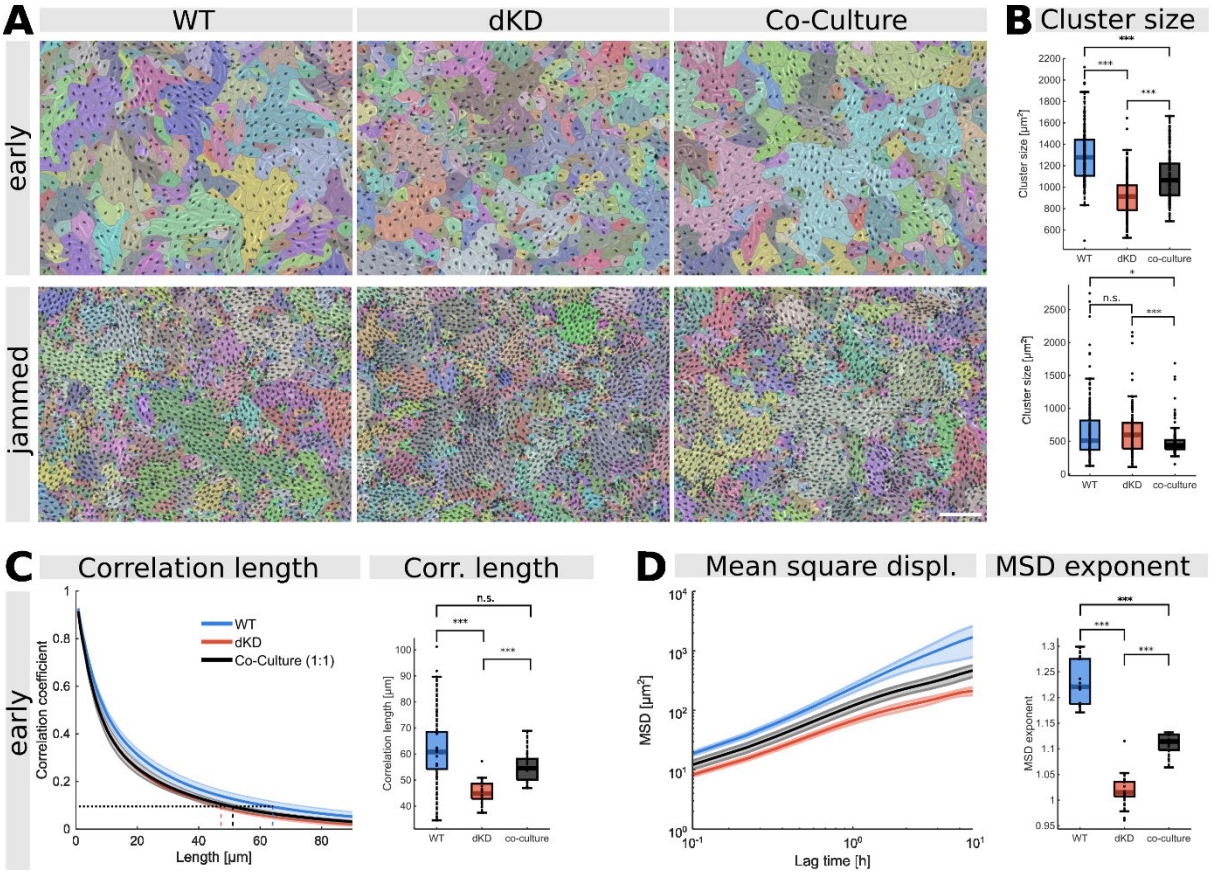

Figure 7. Cluster size, correlation length, and mean square displacements. A) Representative motion cluster maps of WT, dKD, and co-culture (1:1 ratio) with corresponding cell outlines obtained by Cellpose at early (between 5 h and 10 h after seeding) and jammed (between 30 h and 35 h after seeding) phases of the observation period. The arrows represent the motion of individual cells. Cells with similar directionality are grouped into a cluster with the same color. Scale bar: 150 µm. B) Box plot of the cluster sizes of early (upper plot) and jammed (lower plot) states. Each point represents the average cluster sizes of a single frame. C) Spatial correlation of velocity for early times. Vertical dashed lines indicate the corresponding correlation lengths (see right plot). D) Mean square displacements (MSD) of WT cells, dKD cells, and co-culture at early times. The corresponding MSD exponents are shown next to it.